Università degli Studi di Padova

DIPARTIMENTO DI DIPARTIMENTO DI FISICA E ASTRONOMIA GALILEO GALILEI
Corso di Laurea magistrale in Astronomia

Master Thesis

The influence of rotation on black holes formation

Candidato:
Enrico Montanari

Relatore:
Prof. Michela Mapelli

Correlatore:
Dr. Mario Spera

Anno Accademico 2018-2019

Influence of stellar rotation on black holes formation

thesis presented

by

Enrico Montanari

to

Dipartimento di Fisica e Astronomia

Thesis advisor: Michela Mapelli Enrico Montanari

Influence of stellar rotation on black holes formation

Abstract

Gravitational wave (GW) observations by ground based GW interferometers proved the existence of black hole (BH) binary systems. In my thesis, I have investigated the influence of massive star rotation on the formation of neutron stars (NSs) and BHs, by incorporating an updated grid of rotating massive stellar models into SEVN, our new population-synthesis code. These models cover a range of masses between 13 and 120 $M_{\odot}$, four metallicities ([Fe/H]= 0, -1, -2, -3) and three different initial rotation velocities (i.e. 0, 150 and 300 km/s). I find that rotating stars enter (pulsational) pair instability at lower ZAMS mass and thus produce lower-mass BHs, especially at low metallicity. This result is crucial for interpreting GW data.

”Dobby is *free*”

-J.K. Rowling, Harry Potter and the Chamber of Secrets

Contents

1

Introduction and aims

The following section presents the scientific background and the goals of my thesis work.

In the past few years, thanks to LIGO and Virgo interferometers, eleven gravitational wave (GW) sources have been detected (The LIGO Scientific Collaboration et al., 2018). This network of ground-based interferometric detectors is sensitive to GWs from the inspiral, merger and ringdown of compact binary coalescence. These observations provided evidence of the existence of binary black hole (BBH) systems that spiral in and merge within the age of the Universe. Before this groundbreaking discovery, the observational proofs of the existence of stellar BHs come from micro-lensing and X-ray binaries (XRBs), where a compact object accretes matter from a stellar companion. The mass measurement for XRBs relies on the orbital period and the radial velocity of the system. When the mass of the compact object is found to exceed 3 $M_{\odot}$, then the XRB is considered to host a BH. There is about a dozen of known BH XRBs with dynamical mass measurement confirmed, the majority of them host a BH with mass between 5 - 10 $M_{\odot}$,

while some have masses of 10-20 $M_{\odot}$ (Abbott et al., 2016). XRBs have been observed in low stellar density galactic fields and in globular clusters (GCs), even though dynamical mass measurements for systems in GCs have not been possible. Instead GWs from compact binaries carry information about the properties of the source such as the masses and spins. Coherent Bayesian analyses using advanced waveforms allow to measure several physical parameters of the source, with 90% credibility. Moreover GW detections do not depend on the environment in which the source is located, they depend only on the sensitivity of the interferometers. A list of the eleven sources detected so far is presented in table 1.0.1, in which some of the most relevant parameters are also displayed. As it can be seen, BHs from GW observations are heavier than BHs which are part of XRBs. It is important to underline that new data will soon be added to these detections thanks to the third observation run ($O3$) by LIGO and Virgo, and in the near future new ground-based detectors with improved sensitivity will be operational.

In general, the mass of a compact object is expected to strongly depend on the evolution of its progenitor and also on the final supernova (SN) mechanism (Spera and Mapelli, 2017). In the last few years pre-SN models have been upgraded with improved stellar wind recipes and with the addition of stellar rotation effects. In particular, this last feature is really important to determine the pre-SN mass, which plays a key role in understanding the final fate of a star. As a matter of fact stellar rotation affects the evolution of a star in many ways: externally it changes the luminosity, while internally it enhances the chemical mixing. Although theoretical effects have been studied, there is no study about the consequences of rotation on BHs formation. For this reason in this thesis I investigated how stellar rotation affects the mass of the compact objects. For this purpose I used a grid of pre-SN models (Limongi and Chieffi, 2018) and evolved them through time with SEVN (Stellar EVolution for N-body), our new population-synthesis code (Spera et al., 2018).

Table 1.0.1: List of some selected parameters of the GW sources detected. The columns show source frame component masses m_i and chirp mass $\mathcal{M}$, dimensionless effective aligned spin χ_{eff}, final source frame mass M_f, luminosity distance d_L and redishift z (calculated from the lumimosity distance). (The LIGO Scientific Collaboration et al., 2018)

Event	$m_1/M_\odot$	$m_2/M_\odot$	$\mathcal{M}/M_\odot$	χ_{eff}	$M_f/M_\odot$	d_L/Mpc	z
GW150914	$35.6^{+4.8}_{-3.0}$	$30.6^{+3.0}_{-4.4}$	$28.6^{+1.6}_{-1.5}$	$-0.01^{+0.12}_{-0.13}$	$63.31^{+3.3}_{-3.0}$	430^{+150}_{-170}	$0.09^{+0.03}_{-0.03}$
GW151012	$23.3^{+14.0}_{-5.5}$	$13.6^{+4.1}_{-4.8}$	$15.2^{+2.0}_{-1.1}$	$0.04^{+0.28}_{-0.19}$	$35.7^{+9.9}_{-3.8}$	1060^{+540}_{-480}	$0.21^{+0.09}_{-0.09}$
GW151226	$13.7^{+8.8}_{-3.2}$	$7.7^{+2.2}_{-2.6}$	$8.9^{+0.3}_{-0.3}$	$-0.18^{+0.20}_{-0.19}$	$20.5^{+6.4}_{-1.5}$	440^{+180}_{-190}	$0.09^{+0,04}_{-0.04}$
GW170104	$31.0^{+7.2}_{-5.6}$	$20.1^{+4.9}_{-4.5}$	$21.5^{+2.1}_{-1.7}$	$-0.04^{+0.17}_{-0.20}$	$49.1^{+5.2}_{-3.9}$	960^{+430}_{-410}	$0.19^{+0.07}_{-0.08}$
GW170608	$10.9^{+5.3}_{-1.7}$	$7.6^{+1.3}_{-2.1}$	$7.9^{+0.2}_{-0.2}$	$0.03^{+0.19}_{-0.07}$	$17.8^{+3.2}_{-0.7}$	320^{+120}_{-110}	$0.07^{+0.07}_{-0.08}$
GW170729	$50.6^{+16.6}_{-10.2}$	$34.3^{+9.1}_{-10.1}$	$35.7^{+6.5}_{-4.7}$	$0.36^{+0.21}_{-0.25}$	$80.3^{+14.6}_{-10.2}$	2750^{+1350}_{-1320}	$0.48^{+0.19}_{-0.20}$
GW170809	$35.2^{+8.3}_{-6.0}$	$23.8^{+5.2}_{-5.1}$	$25.0^{+2.1}_{-1.6}$	$0.07^{+0.16}_{-0.16}$	$56.4^{+5.2}_{-3.7}$	990^{+320}_{-380}	$0.20^{+0.05}_{-0.07}$
GW170814	$30.7^{+5.7}_{-3.0}$	$25.3^{+2.9}_{-4.1}$	$24.2^{+1.4}_{-1.1}$	$0.07^{+0.12}_{-0.11}$	$53.4^{+3.2}_{-2.4}$	580^{+160}_{-210}	$0.12^{+0.03}_{-0.04}$
GW170817	$1.46^{+0.12}_{-0.10}$	$1.27^{+0.09}_{-0.09}$	$1.186^{+0.001}_{-0.001}$	$0.00^{+0.02}_{-0.01}$	≤ 2.8	40^{+10}_{-10}	$0.01^{+0.00}_{-0.00}$
GW170818	$35.5^{+7.5}_{-4.7}$	$26.8^{+4.3}_{-5.2}$	$26.7^{+2.1}_{-1.7}$	$-0.09^{+0.18}_{-0.21}$	$59.8^{+4.8}_{-3.8}$	1020^{+430}_{-360}	$0.20^{+0.07}_{-0.07}$
GW170823	$39.6^{+10.0}_{-6.6}$	$29.4^{+6.3}_{-7.1}$	$29.3^{+4.2}_{-3.2}$	$0.08^{+0.20}_{-0.22}$	$65.6^{+9.4}_{-6.6}$	1850^{+840}_{-840}	$0.34^{+0.13}_{-0.14}$

2

Theoretical background

The following section aims to present the theoretical background of my thesis work. In particular I will focus on the effects of stellar rotation on the evolution of massive stars in section 2.1, in section 2.2 I will describe stellar winds, while in section 2.3 I will illustrate the theoretical models of SNe.

2.1 Physical effects of rotation

In a rotating star, centrifugal forces reduce the effective gravity according to the latitude and introduce deviations from sphericity. Therefore the four equations of stellar structure need to be modified. In order to keep the treatment of this topic simple enough, Maeder and Meynet (2000) adopted the so called *shellular rotation*, which is differential rotation with Ω constant on isobars. This semplification allows the models to be 1-D, so the computation is faster.

A reduced effective gravity affects the radiative flux $\vec{F}$: according to the von Zeipel theorem, the

radiative flux $\vec{F}$ in a uniformly rotating star is proportional to the local effective gravity g_{eff}. If the star is not close to the Eddington limit, we can write $\vec{F}$ as

$$\vec{F} = -\frac{L(P)}{4\pi G M_*(P)} \vec{g_{eff}} \tag{2.1}$$

where $M_* = M(1 - \frac{\Omega^2}{2\pi G\bar{\rho}})$, $L(P)$ is the luminosity on an isobar and g_{eff} is the effective gravity.

2.1.1 Transport of angular momentum and chemical elements

Inside a rotating star the angular momentum is transported by convection, turbulent diffusion and meridional circulation. Convection, i.e., the turbulent turnover of matter in a medium heated from below, is a basic mechanism of energy transport in stars together with radiative transfer. In addition, it produces fast mixing of the chemical elements, generally leading to the chemical homogeneity of the convective regions. Convection transports also the angular momentum, thus influencing the evolution of rotation. Diffusion is a transport process which results from chaotic motions. In diffusion processes arising from hydrodynamical instabilities, only the quantities with a gradient are transported. This is the case of gradients of chemical composition and of angular momentum which are smoothed by diffusion. Meridional circulation arises from a thermal imbalance which generates global circulation motions in the meridional plane. In section 2.1.3 further details are presented. For *shellular rotation* the equation of transport of angular momentum in the vertical direction is (in lagrangian coordinates)

$$\rho \frac{d}{dt}(r^2\Omega)_{M_r} = \frac{1}{5r^2}\frac{\partial}{\partial r}(\rho r^4 \Omega U(r)) + \frac{1}{r^2}\frac{\partial}{\partial r}(\rho D r^4 \frac{\partial \Omega}{\partial r}) \tag{2.2}$$

where $\Omega(r)$ is the mean angular velocity at level r, $U(r)$ the vertical component of the meridional circulation velocity and D the diffusion coefficient due to the sum of the various turbulent diffusion processes. The factor $\frac{1}{5}$ comes from the integration in latitude. If both $U(r)$ and D are zero, we just have the local conservation of the angular momentum $r^2\Omega = const.$, for a fluid element in case of contraction or expansion. The solution of 2.2 gives the *non-stationary solution* of the problem. It is useful to associate some characteristic timescale to the process of meridional

circulation and diffusion,

$$t_{circ} \simeq \frac{R}{U}, \quad t_{diff} \simeq \frac{R^2}{D} \tag{2.3}$$

where R is the radius of the star. These timescales can be compared with the nuclear timescale to understand the relative importance of the transport processes in the considered nuclear phases. At the beginning of the main sequence (MS), t_{circ} is short with respect to the nuclear evolution time; in this situation equation 2.2 admits a *stationary solution*:

$$U(r) = -\frac{5D}{\Omega}\frac{\partial \Omega}{\partial r} \tag{2.4}$$

This solution is the local conservation of angular momentum, namely it expresses that the inward flux of angular momentum transported by meridional circulation is equal to the outward diffusive flux of angular momentum. Diffusion and advection are physically quite different: diffusion brings a quantity from where this quantity is abundant to other places where there is a scarcity, advection instead is the transport of a quantity or a physical property by the flow of a fluid. Equation 2.2 is subject to boundary conditions at the edge of the core and at the stellar surface. At both places, this condition is usually $\frac{\partial \Omega}{\partial r} = 0$ with the assumptions of solid body rotation for the convective core and $U = 0$.

2.1.2 Transport of chemical elements

The transport of chemical elements is also governed by a diffusion-advection equation like equation 2.2. However, if the horziontal component of the turbulent diffusion is large, the vertical advection of the elements can be treated as a simple diffusion with coefficient D_{eff},

$$D_{eff} = \frac{|rU(r)|^2}{30 D_h}, \tag{2.5}$$

where D_h is the coefficient of horizontal turbulence. Equation 2.5 expresses that the vertical advection of chemical elements is severely inhibited by the strong horizontal turbulence characterized by D_h. The sum of D_{eff} and D from equation 2.2 gives D_{mix} which is the coefficient

for the chemical mixing in the star. Its characteristic time is therefore

$$t_{mix} \simeq \frac{R^2}{D_{mix}} \tag{2.6}$$

2.1.3 Meridional circulation

Meridional circulation arises because the equipotentials, or surface levels, are closer to each other in the polar regions and more spaced in the equatorial regions due to the centrifugal force. The radiative flux is proportional to the effective gravity, see equation 2.1. Thus, if there is an excess of flux along the polar axis there is also a deficiency near the equatorial plane. This thermal imbalance generates global circulation motions in the meridian plane. The velocity of meridional circulation is the main quantity characterizing this effect, and is developed into two different components:

$$U(r) = U_2(r)P_2(\cos\theta)\mathbf{e}_r + V_2(r)\frac{dP_2(\cos\theta)}{d\theta}\mathbf{e}_\theta \tag{2.7}$$

$U_2(r)$ is the amplitude of the radial component, $V_2(r)$ is the amplitude of the horizontal component of the meridional circulation velocity, P_2 is the second order Legendre polynomial and θ is colatitude. The first term can be written as:

$$U_2(r) = \frac{P}{\overline{\rho}C_P\overline{T}(\nabla_{ad} - \nabla + \frac{\varphi}{\delta}\nabla_\mu)}\left[\frac{L(r)}{M_*(r)}(E_\Omega + E_\mu) + \frac{C_P}{\delta}\overline{T}\frac{\partial\Theta}{\partial t}\right] \tag{2.8}$$

Equation 2.8 is called Eddington-Sweet circulation, where P is pressure, C_p is specific heat at constant pressure, T is temperature, ∇_{ad} is the adiabatic gradient, ∇ is the temperature gradient, ∇_μ is the mean molecular weight gradient, $L(r)$ is the luminosity of the star at radius r, E_Ω and E_μ are terms depending on the Ω- and μ-distributions respectively, $M_*(r)$ is the mass of the star at radius r and Θ is the density fluctuations. All the various quantities P, $\overline{T}$, $\overline{\rho g}$, E_Ω, etc.. are taken at the considered level r, while the overlined terms are the average density over the considered isobar. The term E_μ is different from zero only in regions where there is a μ gradient, which shows the need to accurately describe the μ profile in stellar interiors. E_μ is significant in regions surrounding the convective core, when there is one, and in the center of solar-type stars. The term E_Ω in the case of uniform rotation is positive, which means that equation 2.7 is going up along the polar axis and descending along the equatorial plane, a pattern which transports the angular

momentum inward. Close to the surface things change because of the Gratton-Öpik circulation cell, that turns the circulation in the opposite direction and which makes an outward transport of angular momentum. This plays an important role in stellar evolution by pumping angular momentum in the interior and increasing the surface rotation. If the metallicity is low the cell is absent and this leads to a large mixing of chemical elements. In figure 2.1.1 it is represented the inner structure of a star with the two circulation cells.

2.1.4 Properties of Meridional Circulation

The circulation timescale t_{circ}, also called the Eddington–Sweet timescale t_{ES}, is of the order of the stellar radius divided by 2.8,

$$t_{ES} \approx \frac{R}{U_2(R)} \approx \frac{t_{KH}}{\Omega^2 R^3/(GM)} \tag{2.9}$$

where t_{KH} is the Kelvin–Helmholtz timescale. Thus, the circulation timescale is of the order of t_{KH} divided by the ratio of the centrifugal force to gravity parameter. Hence in a rotating star t_{ES} is some multiple of t_{KH}. Taking as example the star in figure 2.1.1, $t_{ES} = 5 \times 10^5$yr and its MS lifetime is approximately 9×10^6 yr. This means that the transport of angular momentum by circulation is efficient during the MS phase. The transport of chemical elements is slowed down by horizontal turbulence. The order of the overall problem can be extimated from 2.8: as a matter of fact E_Ω contains up to the second derivative of Θ, but since Θ itself depends from the derivative of Ω, therefore $U_2(r)$ depends on the third derivative of Ω. Through the equation of transport of angular momentum we can observe that the evolution of Ω depends on the derivative of $U_2(r)$. Thus the whole time evolution of Ω depends on the fourth derivative of Ω, i.e.,

$$t_{ES}\frac{\partial \Omega}{\partial t} \sim R^4 \frac{\partial^4 \Omega}{\partial r^4} \tag{2.10}$$

This implies that the differences of rotation brought about by circulation enter within a time δt over a distance δr into a radiative zone with

$$\delta r = t^{1/4} \tag{2.11}$$

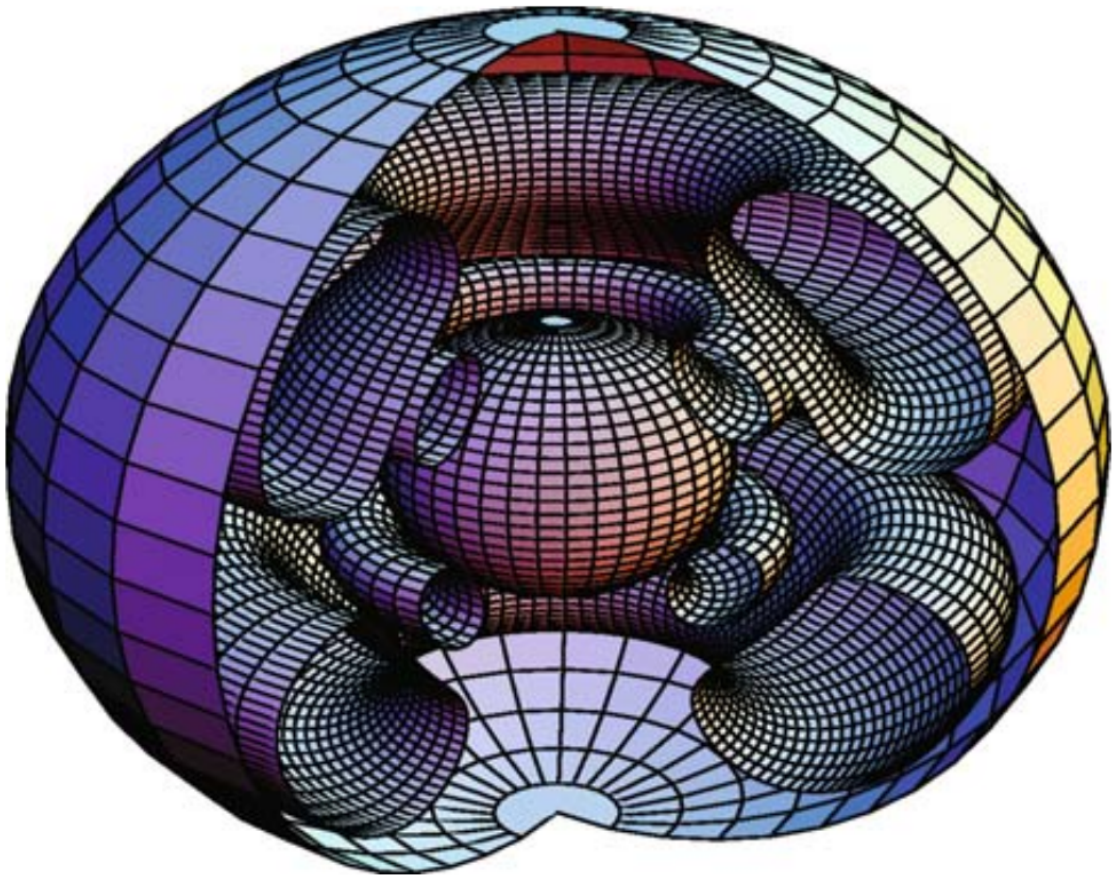

Figure 2.1.1: Schematic structure with stream lines of meridional circulation as a function of M_r in a rotating 20 $M_\odot$ model of 5.2 $R_\odot$ with Y = 0.30, Z = 0.02 and v_{ini} = 300 km/s at the beginning of the MS phase. In the upper hemisphere on the right section, matter is turning counterclockwise along the outer stream line and clockwise along the inner one. The inner sphere is the convective core. It has a radius of 1.7 $R_\odot$ (Maeder, 2009).

consequently, the progression of the differences of Ω caused by circulation needs much more time for larger regions.

2.1.5 T and μ circulation pattern

The time-evolution of rotation requires a good understanding of circulation patterns and therefore on how angular momentum is transported. The derivatives of Ω and μ in E_Ω and E_μ greatly influence the circulation. It is worthwhile mentioning that the star at the beginning of its life rotates as a solid body. In the case analysed here there is an excess of temperature T along the polar axis. $U_2(r)$ is positive, therefore matter enriched in helium climbs up along the polar axis, making a positive μ excess in regions with T excesses. After rising upwards, the hot material will cool down and sink down. The μ currents are opposed to the driving effect of circulation, they in fact tend to inhibit it and for this reason they are called μ barriers. In the outer layer, the Gratton-Öpik term produces an inverse circulation due to the lower density. As evolution proceeds, rotation becomes differential and the star becomes baroclinic (all the quantities varies with colatitude on the same isobar). Despite the higher T near the polar axis, the density fluctuations make the matter of the large inner cell to rise in the equatorial plane and to descend along the polar axis.

It is important to highlight the key-role that the Gratton-Öpik term plays, since it can change the sign of $U_2(r)$; if $U_2(r) > 0$ the circulation goes up along the polar axis and descend in the equatorial plane, transporting angular momentum inward, while a negative $U_2(r)$ makes an outward transport of angular momentum. The sign of $U_2(r)$ drastically changes the evolution of a star because the transport of angular momentum influences the steepness of the Ω gradient, which in turn may produce shears favouring the mixing of the chemical elements. At low metallicity Z the stars are more compact,as a consequence the density remains relatively high in stellar envelopes and thus the Gratton-Öpik term is very weak. The consequences are that $U_2(r)$ in the outer layer is low, the outwards transport of angular momentum is low and this favours a steep internal Ω gradient with a significant gradient up to the stellar surface. High gradients are responsible for strong chemical mixing, and as a consequence the various model properties, such as size of the core and lifetimes, are largely influenced. This shows that meridional circulation is the major ingredient of proper evolutionary models.

2.2 Mass loss and Rotation

In massive stars, mass loss results from stellar winds driven by the strong radiation pressure of very luminous stars, which pushes the mass outside. The main transfer of momentum is due to the absorption of the stellar radiation by stellar lines. Red Super Giants (RSGs) also experience strong mass loss, due mostly to the absortion and diffusion of radiation by dust and to pulsations. In massive stars and in the advanced evolution of intermediate mass stars, mass loss is a dominant effect influencing all the outputs of stellar evolution and nucleosynthesis (Maeder, 2009). The line absorptions in stellar atmospheres transfer the radiation momentum to the stellar matter accelerating it outward. The momentum is mainly transferred by UV photons in resonance lines of Fe and CNO elements. Thus the radiatively driven stellar winds are efficient mainly in hot bright stars, like OB stars, and with enough heavy elements. The simplified general theory asserts that the outward mass flow is determined by the continuity equation and the momentum conservation. In particular

$$\begin{aligned} \dot{M} &= 4\pi r^2 \rho v = const. \\ v\frac{dv}{dr} &= -\frac{GM}{r^2} + \frac{1}{\rho}\frac{dP}{dr} + g_{rad} \end{aligned} \tag{2.12}$$

where $\dot{M}$ is the time derivative of the mass, r is the radius of the star, ρ is the density, P the pressure and g_{rad} is the radiative acceleration sum of the acceleration from continuous absorption by electron scattering ($g_{rad,es}$) and from spectral lines ($g_{rad,L}$). The term $g_{rad,L}$ depends on optical depth τ, which depends from metallicity Z. This simplified theory uses an analytical approach in the single scattering limit (Abbott, 1980). Vink et al. (2001) instead included multiple scattering effects which led to major upgrade in stellar wind recipes. The main results concerning my thesis are the dependency of mass loss from the effective temperature T_{eff} of the stars, in particular:

$$\begin{aligned} \log \dot{M} = &-6.688 + 2.210 \log(L_*/10^5) - 1.339 \log(M_*/30) - 1.601 \log(\frac{v_\infty / v_{esc}}{2.0}) \\ &+ 1.07 \log(T_{eff}/20000) + 0.85 \log(Z/Z_\odot) \end{aligned} \tag{2.13}$$

$$\begin{aligned}\log \dot{M} = &-6.697 + 2.194 \log(L_*/10^5) - 1.313 \log(M_*/30) - 1.226 \log(\frac{v_\infty/v_{esc}}{2.0}) \\ &+ 0.933 \log(T_{eff}/40000) - 10.92 \big[\log(T_{eff}/40000)\big]^2 + 0.85 \log(Z/Z_\odot)\end{aligned} \tag{2.14}$$

where L_* is the luminosity of the star, M_* is the mass of the star, v_∞ is the wind velocity to infinity and v_{esc} is the escape velocity. Equation 2.13 counts for effective temperature between 12500 K $\leq$ T $\leq$ 25000 K and v_∞/v_{esc} equal to 1.3 , while 2.14 for 25000 K $\leq$ T $\leq$ 50000 K and v_∞/v_{esc} equal to 2.6. The above dichotomy is due to the bistabilty jump, i.e. a sudden jump in the mass loss rate related to the fact that the iron ions driving the wind recombine at T $\sim$ 25000 K, and again below 12500 K. The dependence of the mass loss rates on metallicity is responsible for differences in the populations of massive stars in galaxies and also for differences in the chemical yields with metallicity. These relations do not account for stellar rotation (mainly the consequences of von Zeipel theorem, see equation 2.1). As a matter of fact rotation introduces anisotropies in stellar winds, because the effective gravity is changing with latitude and thus the polar regions are hotter than the equatorial ones; also the global mass loss rates are increased by rotation. Strong polar winds allow a star to lose lots of mass without losing too much angular momentum, on the contrary, equatorial mass loss removes a lot of angular momentum.

Maeder (2009) included latitudinal variations in mass loss by stellar wind

$$\frac{\Delta \dot{M}}{\Delta \sigma} = A(ac/4)^{1/8} \Big[\frac{L(P)}{4\pi G M_*(P)}\Big]^{\frac{1}{a}-\frac{1}{8}} \frac{g_{eff}^{1-\frac{1}{8}}}{\big[1-\Gamma(\Omega,\theta)\big]^{\frac{1}{a}-1}} \tag{2.15}$$

where A is a parameter which depends from the force multiplier factors k and a, θ is the colatitude, Γ is the Eddington factor. From 2.15 two effects arise:

1. g_{eff} effect: due to higher gravity at the poles of rotating stars, the polar flux is enhanced, while the equatorial flux is smaller.

2. κ effect: when the opacities are not only due to electron scattering, the higher opacities at lower T_{eff} lead to higher k and smaller a at the equator and thus favour equatorial ejections.

Figure 2.2.1 shows two 3D representations of the distributions of the mass loss rates around a very bright star. On the left, where a T_{eff} = 30000 K is assumed, the star is hot enough for the

electron scattering opacity to dominate from pole to equator. Consequently, the distribution of the mass loss rates with θ is shaped only by the g_{eff} effect, which produces the peanut shape of the distribution of the mass loss rates by stellar winds. On the right, a $T_{eff} = 25000$ K is assumed. In this hypothesis it can be observed that in the cooler equatorial region the opacity is higher. This causes an equatorial enhancement of the stellar winds (κ effect) forming a sort of disk in addition to the peanut shape of the g_{eff} effect, which is always present.

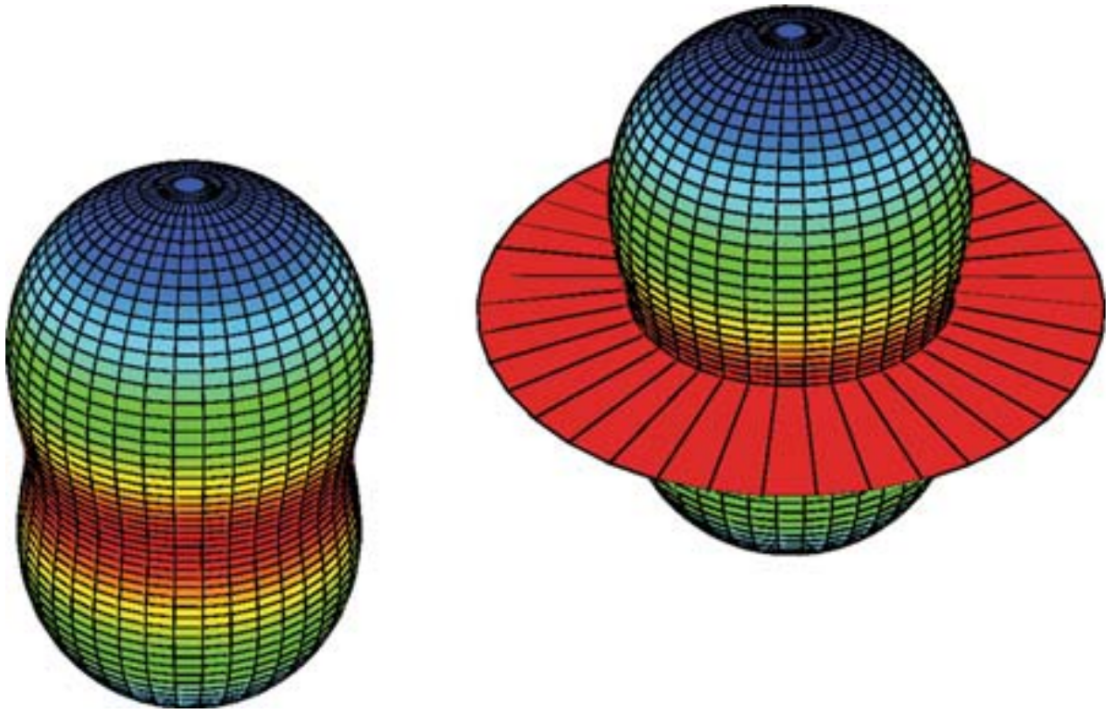

Figure 2.2.1: *Left*:the mass fluxes around a rotating star of 100 $M_{\odot}$ with $10^{6.5}$ $L_{\odot}$ and a ratio of the angular velocity to the break-up angular velocity $\omega = 0.80$, assuming a polar $T_{eff} =$ 30000 K.*Right*: the same star but with $T_{eff} = 25000$ K, the k effect creates a ring ejection. (Maeder, 2009)

2.2.1 Consequences on Evolution

The physics and evolution of massive stars are influenced by mass loss and by rotational mixing. The rotation velocities of O-type stars decrease by 30% or more during the MS phase due to mass

loss (at solar metallicity and expansion, implying that the initial values are even larger. Both mass loss and rotational mixing influence the model's outputs such as tracks in the HR diagram, lifetimes, abundances, chemical yields and supernova progenitors.

2.2.2 External differences

The overall mass reduction makes the star less luminous; however, the star is overluminous because of its actual mass, since the core mass fraction is larger as an effect of better mixing and that is why the MS duration is more extended. The rotation instead distorts the star, which therefore radiates anisotropically: hotter and brighter at the poles and cooler and fainter at the equator. As evolution proceeds, differential rotation appears (see 2.1.5) and the resulting improved chemical mixing brings some helium out of the convective core into the radiative envelope, slightly increasing its mean molecular weight. The net effect is a larger convective core. The helium enhancement in the envelope lowers its opacity, which increases L and makes the star hotter, favouring a blueward track.

2.2.3 Internal differences

Internally the chemical mixing brings more hydrogen into the core, which leads to a longer MS phase and a more massive helium core. It is worth to mention that the role of mixing and circulation after the main sequence is not particularly important since in massive stars the timescales for mixing and circulation are much larger than the evolutionary timescale during the He-burning phase and the following ones (Maeder and Meynet, 2000). These processes will therefore globally have small effects during the above-mentioned stages.

2.3 Supernova Mechanisms

SNe are stellar explosion during which a star may reach a luminosity of about $10^{10}\ L_{\odot}$. A part of the heavy elements synthesized during the evolution and explosion goes into the remnant (neutron star (NS) or BH), another part is ejected at velocity $\geq 10^4$ km/s. SNe enrich the interstellar medium in the nucleosynthetic products; they also inject kinetic energy in the interstellar medium, compressing the medium and thus favouring new stellar births. Instability processes due

to the mass of the Helium core could greatly enhance the mass loss or even disrupt the whole star.

2.3.1 Pair instability and Pulsational Pair Instability

Massive stars can during their lifetime can grow massive cores; especially if the mass of the star's helium core grows above $\sim 30\,M_\odot$ (but less than $64\,M_\odot$) and its temperature T is $\geq 7 \times 10^8$ K, then the photons produced are so energetic that they produce electron-positron pairs. As a consequence the photon pressure quickly drops causing a sudden collapse before the iron core is formed. This pair production induces a series of disruptive pulsations, which triggers an enhanced mass loss (Woosley, 2017): this mechanism is called pulsational pair instability SN (PPISN). At the end of this instability phase a non-zero remnant is produced, significantly lighter than a case of direct collapse. If the mass of the core m_{core} grows above $64\,M_\odot$, the star collapses and cannot reach a new stable configuration; the collapse triggers an explosive burning of heavier elements, which has disruptive effects. This leads eventually to a complete disruption of the star, leaving no remnant (Woosley, 2017). This mechanism is called pair instability SN (PISN). A visual representation of these two processes can be seen in the right panel of figure 2.3.1, in which the mass of the compact object is shown as a function of the Zero-Age Main Sequence (ZAMS) mass. The upper grey band highlights the effects of PPISNe and PISNe: the first one is responsible for the steep decrease between $\sim 60\,M_\odot$ and $120\,M_\odot$, while the latter causes the absence of compact object between $\sim 120\,M_\odot$ and $\sim 220\,M_\odot$.

2.3.2 Core-Collapse SNe

The mechanisms triggering iron CCSN are still highly uncertain, many models have been presented but there are still open issues. In the final stage of its lifetime the degenerate core of a massive star reaches the Chandrasekhar mass, which is to say that the degeneracy pressure of electrons is not sufficient anymore to support it against collapse. In addition to that, electrons are increasingly removed, as the protons capture them producing neutrons and neutrinos. The core reaches in this way a new state, it is now composed mainly by neutrons and is supported by their degeneracy pressure. This new equilibrium is reached after a collapse which reduces the radius of the core from a few thousands km down to a few tens km in less than a second. The gravitational

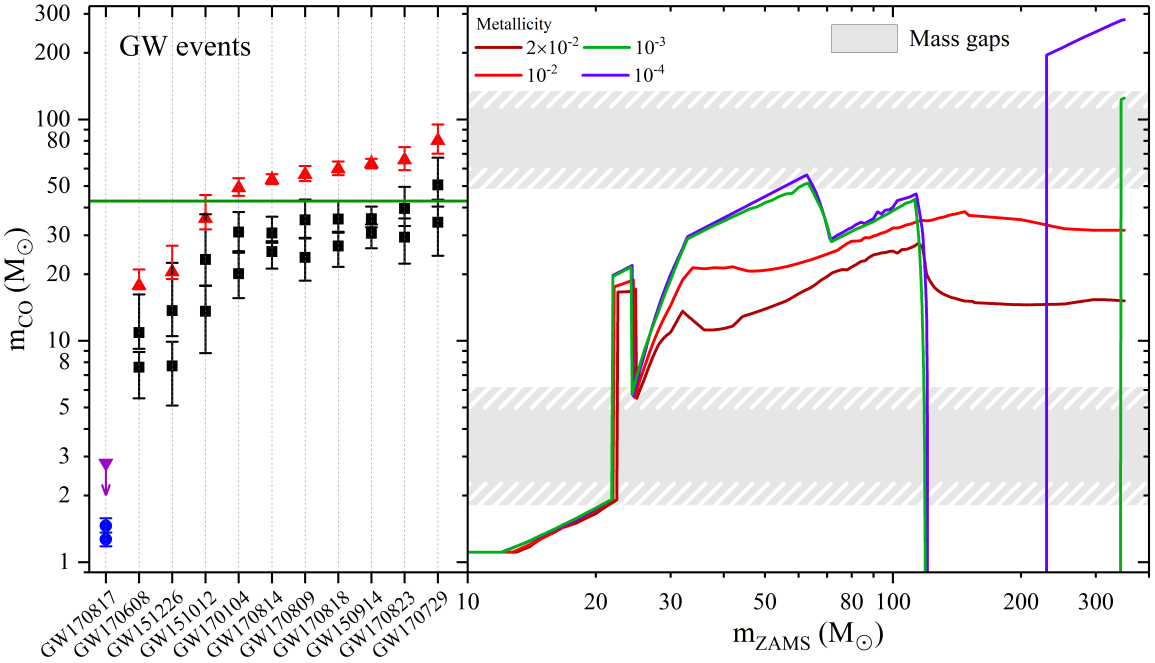

Figure 2.3.1: The left-hand panel shows compact object masses from GW detections in O1 and O2, with the black squares and error bars representing the component masses of the merging black holes and their 90% credible levels, while red triangles represent the mass and associated 90% credible levels of the merger products. In the right-hand panel the predicted compact-object mass is shown as a function of the zero-age main sequence mass of the progenitor star and for four different metallicities of the progenitor star. This model accounts for single stellar evolution from the PARSEC stellar-evolution code for core-collapse SN, and for pulsational-pair instability and pair-instablity SN. The shaded areas represent the lower and the upper mass gaps. (The LIGO Scientific Collaboration et al., 2018)

energy gained from the collapse is $W \sim 5 \times 10^{53}$ erg $(m_{PNS}/1.4M_{\odot})^2 2(10\,\mathrm{km}/R_{PNS})$, where m_{PNS} and R_{PNS} are the mass and radius of a proto-neutron star (PNS)(Mapelli, 2018). The whole issue is how such a gravitational energy is transferred to the stellar envelope triggering the SN explosion.

The most studied mechanism is the convective SN engine, which forms a remnant in three different phases: stellar collapse and bounce, convective engine and post-explosion fallback (Limongi and Chieffi, 2018). The collapse occurs when the stellar core begins to compress under its own weight. The compression leads to electron capture and dissociation of the core elements

into alpha particles, and as a consequence of these processes there are no more thermal and degeneracy pressure support. Therefore the compression is even more accelerated, which in return boosts the rate of electron capture and iron dissociation, leading to a runaway collapse with velocities comparable to the speed of light. The collapse ceases when the core reaches nuclear densities and when nuclear forces dramatically increase the pressure. This sudden halt leads to a bounce shock to move out of the core. The shock moves out until neutrino losses saps its energy reservoir, causing it to stall. The region between the PNS and the shock front might develop a convective region, where energy in the form of neutrinos can be converted into kinetic energy by pushing the convective region outward. A SN explosion occurs if the energy in this convective region can overcome the ram pressure of the infalling material. The time when the energy in the convective region overcomes the ram pressure determines the amount of material accreted onto the PNS during the convective phase.

- **Rapid SN**: if the explosion occurs, it happens within the first 250 ms. It is characterized by an energy above 10^{51} erg, the fallback mass is low. If the PNS exceeds 3 $M_{\odot}$ the star collapses directly to a BH without explosion.

- **Delayed SN**: the explosion can occur over a much longer timescale ($>$ 250ms). It is characterized by an energy lower than the rapid model, but the fall back material is higher.

These two models are characterized by different recipes for the calculation of PNS mass M_{PNS} and mass of the fallback M_{fb}, which I will present in detail in chapter 3.

2.4 Compactness

The dynamics of the post-bounce in a SN can be predicted with the compactness parameter, as a matter of fact it describes the progenitor structure at the core bounce (O'Connor and Ott, 2011). It is defined as

$$\xi_M = \left. \frac{M/M_{\odot}}{R(M)/1000km} \right|_{t=t_{bounce}} \tag{2.16}$$

where M is the baryonic mass, usually set to M =2.5$M_{\odot}$ and $R(M)$ is the radial coordinate that encloses 2.5 $M_{\odot}$. The evaluation of $\xi_{2.5}$ at core bounce is crucial, since this is the only physical and

unambiguous point in core collapse at which one can define a zero of time and can describe the true initial conditions for post-bounce evolution. The fallback time of the matter on the PNS can be expressed as a function of $\xi_{2.5}$ as $t_{BH} \propto (\xi_{2.5})^{-3/2}$ and, hence, progenitors with high values of $\xi_{2.5}$ are those that forms BH the fastest and are the hardest to explode. In figure 2.4.1 time to BH formation is represented as a function of $\xi_{2.5}$, for small $\xi_{2.5}$, the mass element begins its free fall from a large radius and, hence, it takes longer to reach to origin. Previous work (O'Connor and

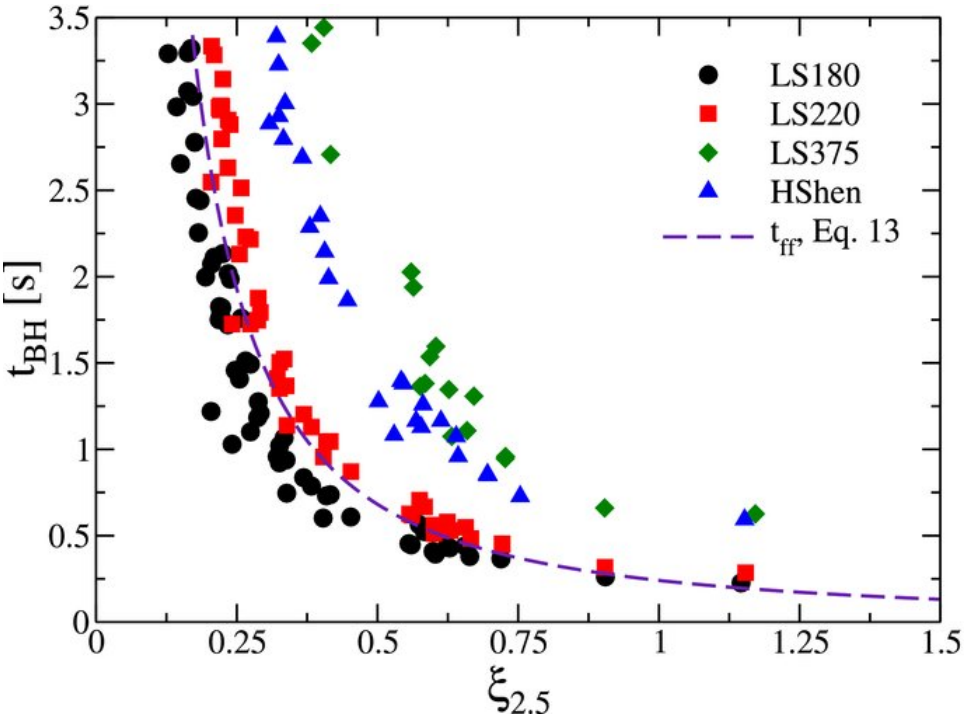

Figure 2.4.1: BH formation time as a function of the bounce compactness ($\xi_{2.5}$) for non rotating models that form BHs within 3.5s of the bounce. Different shapes of the markers refer to different models used in O'Connor and Ott (2011), while the dashed line represents the free fall time to the origin of a mass element located at a baryonic mass coordinate of $2.5 M_{\odot}$. (O'Connor and Ott, 2011)

Ott, 2011) predicts that if the progenitor has $\xi_{2.5} \gtrsim 0.45$, most likely it forms BH without explosion.

3

Models and Code

In this chapter I will present the models created with Frascati Raphson Newton Evolutionary Code (FRANEC) and our population-synthesis code SEVN, which I used to calculate the mass of the compact objects (COs).

3.1 FRANEC models

Limongi and Chieffi (2018) present a wide set of rotating stellar models, thanks to which I analyzed the effects of stellar rotation on BH formation.

3.1.1 General Properties

The physical structure of the star and the chemical composition are described by two different sets of equations, which are coupled together and solved simultaneously by means of a relaxation technique. On the contrary, angular momentum transport is solved separately by means of the

same iterative method. In FRANEC the star is divided in two zones: the atmosphere and the inner region. The former zone has a constant luminosity so that only three equations, instead of four, are solved; moreover in this region the transport of angular momentum by rotation is ignored and the star is assumed to rotate as a solid body together with the external border of the latter. The mass fraction included in the atmosphere is usually fixed at 1% of the current total mass of the star, but, in order to increase the fraction of mass in which the angular momentum is properly transported, during the central H burning phase the fraction is set to 99.99%. This choice cannot be maintained for the whole evolution because when the star turns redward the radius increases considerably and it becomes prohibitive to perform such calculations. This choice is justified by the fact that in the red supergiant (RSG) phase the surface velocity rotation decreases due to angular momentum conservation. In the inner region the borders of the convective zone are defined according to the Ledoux criterion, while the opacity κ coefficients and the mass loss prescriptions are all listed in Limongi and Chieffi (2018) appendix A. Since the rotation is a multidimensional physical phenomenon, its inclusion in a 1D stellar evolution code implies a certain number of assumptions. The calculation of diffusion coefficient for angular momentum f_c and chemical composition f_μ is rich in uncertainties. Even if there is no single solution, after some tests and comparisons with observations, the parameters have been set to f_c = 1.5 and f_μ=0.03.

Parameters	Values
Mass $[M_\odot]$	$13 \leq m_* \leq 120$
Metallicity [Fe/H]	0,-1,-2,-3
V_{eq} [Km/s]	0, 150, 300

Table 3.1.1: All the parameters listed refer to the initial conditions of the models. The initial masses are 13, 15, 20, 25, 30, 40, 60, 80 and 120 $M_\odot$.

In the next section a general overview of the models is presented; for this purpose, table 3.1.1 shows the parameters on which the discussion will be based.

3.1.2 H burning phase

The H burning phase is the longest lasting evolutionary stage of a star. Therefore it is more likely to observe a star in this phase and also the physical phenomena correlated to rotation instabilities have more time to operate. Mass loss significantly affects the evolution of a massive star in the central H burning and its influence increases with the initial mass because of the large dependence of the mass loss rate on the luminosity (see section 2.2). Non rotating solar metallicity models with mass larger than 60 $M_{\odot}$ lose enough H from their envelope to enter the Wolf-Rayet (WR) stage during MS. However the minimum mass required to enter the WR stage for a star does not depend only on the adopted mass loss rate but also, among other things, on the size of the H convective core. In fact, the inclusion of some amount of convective core overshooting makes the evolutionary tracks cooler and brighter compared to the standard ones. This implies an overall higher mass loss and therefore a reduction of the minimum mass to enter the WR stage. The mass of the He core at H core exhaustion increases with the initial mass because it scales with the size of the H convective core, which also scales with the mass of the star. As metallicity decreases mass loss decreases consequently (see equation 2.12), thus for $\left[Fe/H\right] \leq -1$ all non rotating models evolve almost at constant mass in this phase. As represented in figure 3.1.1 the mass of the He core for stars with initial mass $\leq 40 M_{\odot}$ does not depend on metallicity. Instead, stars with initial mass $> 40 M_{\odot}$ significant differences exist due to mass loss.
Rotation has two effects on the evolutionary path of massive star in the Hertzsprung-Russell (HR) diagram: on one side, the lower gravity, due to angular momentum transport and centrifugal force, pushes the star towards lower temperature. On the other side, the increased mean molecular weight in the radiative envelope, due to the rotationally driven mixing, has two consequences:

- the opacity in the H rich mantle lowers, making the star more luminous and more compact and favoring a blueward evolution
- the mass of the convective core increases, making therefore the track brighter and cooler

During H burning phase at solar metallicity rotating stars are on average brighter and hotter than non rotating ones and therefore the increase in mean molecular weight in the envelope of the star

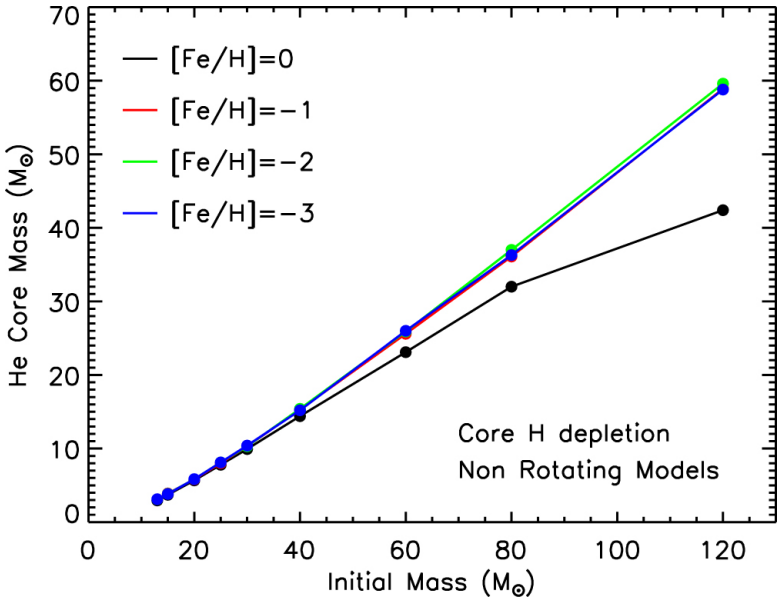

Figure 3.1.1: He core mass at H depletion as a function of the initial mass for non rotating models at various metallicities. (Limongi and Chieffi, 2018)

is the predominant effect. On the other hand, as the metallicity decreases, rotating stars become brighter and cooler than those which do not rotate, hence the reduction of effective gravity mainly controls the evolution (see fig 3.1.2). As mentioned before the mass loss in the H burning phase at solar metallicity increases with initial rotation velocity. Instead, at sub solar metallicities the mass loss rate is negligible. Thus, in general, the minimum mass entering the WNL stage during core H burning decreases with increasing the metallicity and with increasing the initial rotational velocity. In absence of rotation, the mixing of matter occurs only where thermal instabilities (convection) grow. The presence of rotation adds mixing also in thermally stable (radiative) regions. Once again it is useful to stress on the effects of rotation driven mixing: a better mixing leads to a longer H core burning lifetime, therefore the mass of He core will be larger at H exhaustion and the surface abundance of ^{14}N is enhanced. The general trend is that, for any fixed initial mass, the higher the initial rotation velocity, the greater the M_{He} at H depletion (see fig 3.1.3); this holds as long as the mass loss is not efficient enough to reduce substantially the total mass of the star, for instance fast rotating models with $M > 40 M_{\odot}$ at solar metallicity or

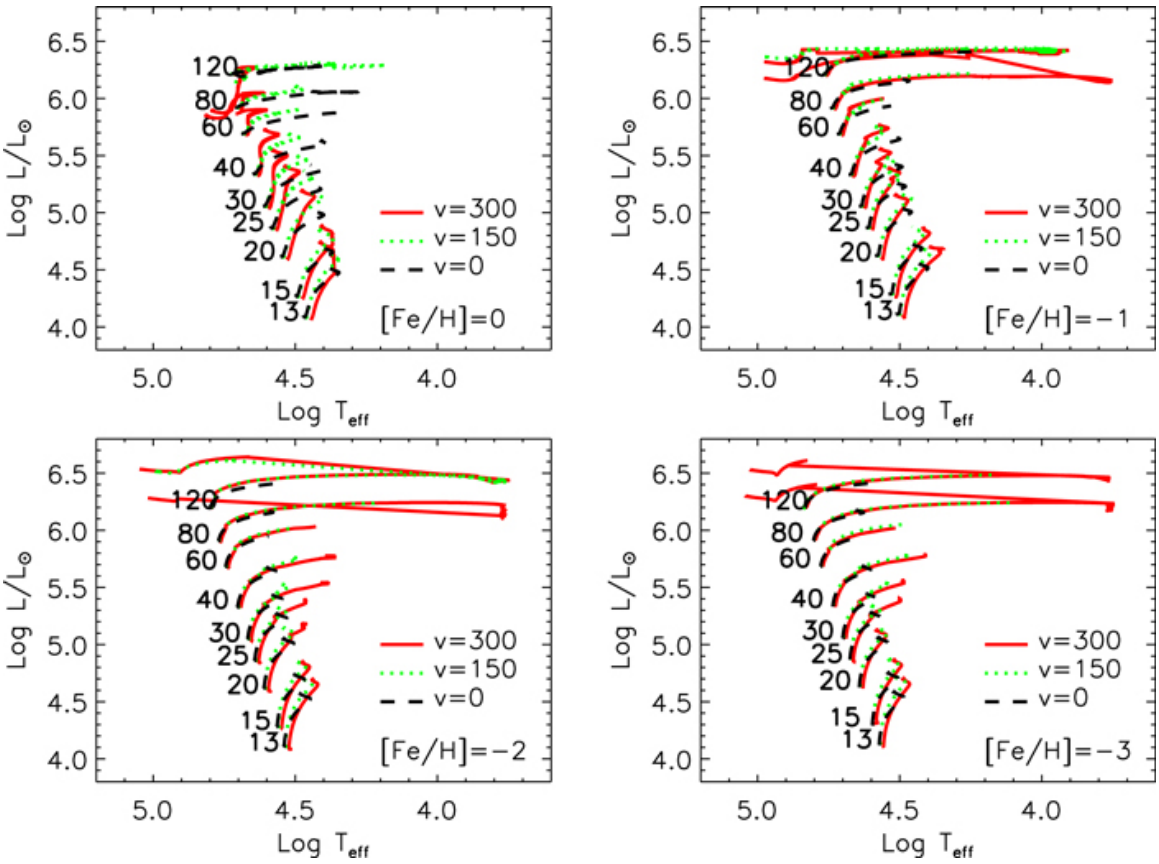

Figure 3.1.2: Evolutionary tracks in the HR diagram of all the computed models during the core H burning phase at different metallicities. Dashed lines refer to non rotating models, dotted and solid to rotating ones (Limongi and Chieffi, 2018).

with M >60 $M_{\odot}$ with $\left[\mathrm{Fe/H}\right]$=-1 or less.

3.1.3 Core He Burning

The life of a star beyond the central H burning depends on many factors:

- the He core contracts in order to reach a new state of equilibrium;
- the H rich mantle expands towards a Red Super Giant (RSG) configuration;
- the He core mass;

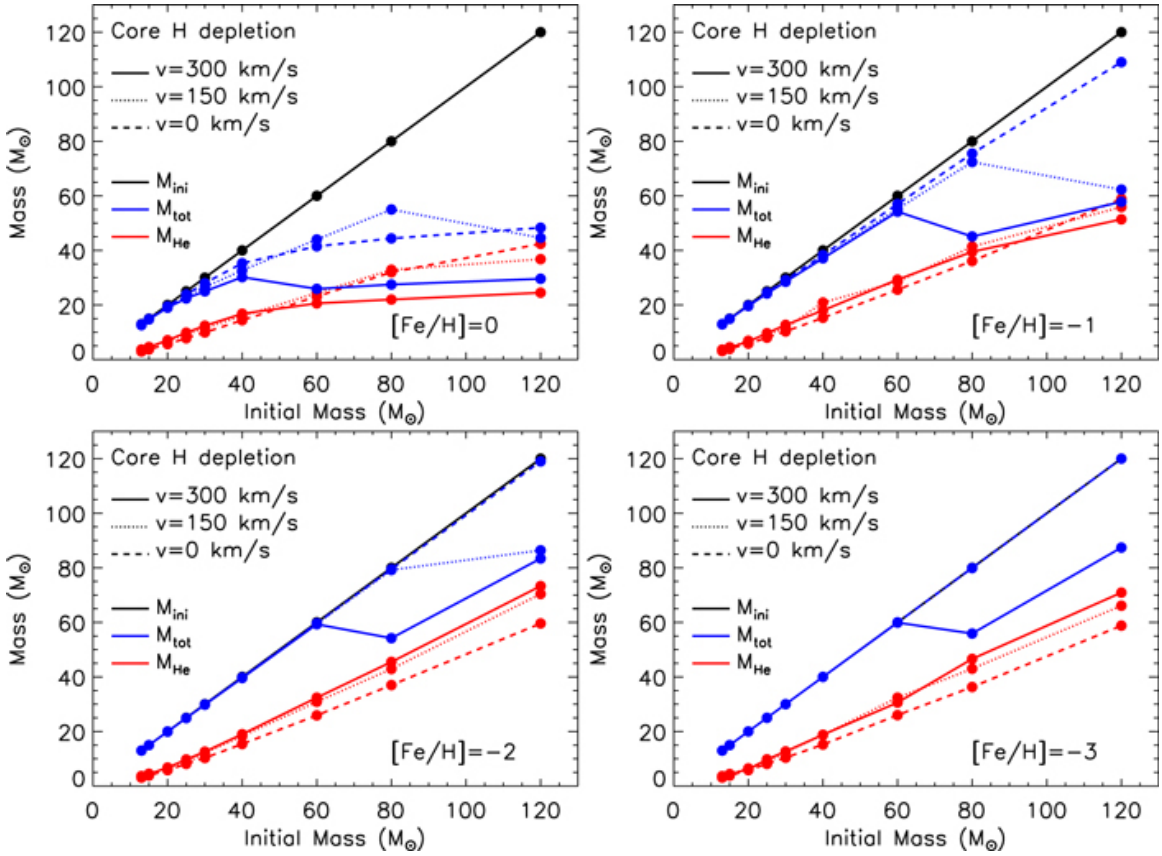

Figure 3.1.3: Total mass, in blue, and He core mass, in red, at core H depletion as a function of the initial mass for various metallicities and different initial rotation velocities (Limongi and Chieffi, 2018).

- the efficiency of mass loss in this phase.

Non rotating models behave differently based on metallicity: at $[\mathrm{Fe/H}] = 0$ models start the core He burning as RSGs, with the only exception of the 120 $M_\odot$ that loses enough mass to become a WR during the core H burning phase. Because of this redward excursion, stars with M $\gtrsim$ 40 $M_\odot$ approach the Eddington luminosity and lose a substantial fraction of the envelope, then evolve to a Blue Super Giant (BSG) and become WRs. Less massive stars reach the critical temperature for the dust driven winds to become efficient. However, only stars with mass M $\geq$ 15 $M_\odot$ have a central He abundance sufficiently high that allows them to lose enough of the H-rich envelope and become first a BSG, and then a WR. Stars with mass M $\leq$ 15 $M_\odot$ stay RSG during

the whole core He burning phase. At $\left[\mathrm{Fe/H}\right]$ = -1 all non rotating models stars with M $\geq$ 60 $M_{\odot}$ expand quickly after the central H exhaustion but, because of the enormous mass loss, they do not reach the Eddington luminosity and then become WRs. Stars with mass between 30 and 60 $M_{\odot}$ ignite ad burn He as BSGs without entering at all the WR phase because of the modest mass loss. Regarding stars with mass M $\leq$ 30 $M_{\odot}$, they ignite and burn He in the core as RSGs, but at this metallicity they do not trigger the formation of dust, therefore they remain RSG during all the He burning phase. At $\left[\mathrm{Fe/H}\right]$ = -2 and -3 the evolution is clear: all non rotating stars ignite and burn He in the core as BSGs. At these metallicities no WRs nor RSGs are expected during this stage of evolution.

The situation in the rotating models becomes even more complex because its effect on the evolution of a star depends on its metallicity and mass. As in the non rotating case, at $\left[\mathrm{Fe/H}\right]$=0, the models can become WR during the core H burning phase and hence burn He in the core as BSGs; also, they can approach their Eddington luminosity during the redward excursion, evolve toward a BSG configuration and burn He in the core as WR stars; or even they can move close their Hayashi track, enter the dust driven wind stage and then turn again to the blue, sometime during the He burning phase. The basic rule is that the higher the initial rotation velocity the lower the limiting masses that divide these three mass intervals. For this metallicity, all rotating models end their He burning lifetime as WR because since they all are pushed beyond the threshold temperature for dust driven winds early enough to have time to lose most of their mantle and turn blue again. At metallicities $\left[\mathrm{Fe/H}\right] \leq -1$ the quite complex interplay between metallicity and rotation does not lead any more to a strictly monotonic trend with the mass. Models can evolve through different paths:

- they can move redward toward the Hayashi track on a thermal timescales, lose a substantial amount of mass because the stars approach their Eddington luminosity, turn to the blue and burns He as WR stars;

- they ignite He as BSGs, move redward while core He burning goes on, become RSGs, turn to the blue sometime during core He burning and become WR stars;

- they ignite He as BSG, move redward on a nuclear timescale, reaching eventually the RSG phase when the central He abundance is more than halved;

- they ignite and burn He as RSGs.

The basic rule in this case is that, on average, the limiting masses that divide the above mentioned mass intervals decrease by increasing the initial rotation velocity and by decreasing the initial metallicity. Note that at these metallicities no model crosses the temperature threshold for the activation of the mass loss due to the dust formation.

The mixing of the chemicals due to the rotation induced instabilities has essentially two basic consequences: the increase of the CO core mass and the exchange of matter between the two active burning regions. These lead to an increase of the mass of the CO core with the rotation, moreover the smaller the mass the larger the increase. Such a trend is due to the combination of two different effects: the He burning lifetime scales inversely with the He core mass, so that the smaller the mass the longer the secular instabilities may operate, and the mass trend is performed on models with a constant initial equatorial rotation velocity. The general direct scaling of the CO core with the initial rotation velocity fails when the He core mass is eroded by mass loss. In these cases the core feels a smaller He core mass and the convective core shrinks accordingly. At $\left[\mathrm{Fe/H}\right]$ = 0 and -1 the most massive rotating stars lose much more mass than their non rotating counterparts and this explains why in these cases the final CO core scales inversely with the initial rotation velocity.

At solar metallicity, rotation roughly doubles the CO core mass of the less massive stars but its influence on M_{CO} progressively reduces as the mass increases, becoming almost negligible for stars with M $\leq$ 40 $M_{\odot}$. In the more massive models with initial rotation velocity v = 300 km/s, the global effect of mass loss overcomes the effect of rotation, resulting in a reduction of CO core mass in rotating models up to $\sim$ 30 – 40 % for the 120 $M_{\odot}$. At metallicities lower than solar, mass loss reduces dramatically and therefore its effect on the CO core mass becomes progressively negligible. The reason is obviously that the evolution of the star after core He depletion is essentially driven by the mass of the He core. An obvious consequence of the increase of the CO core with rotation is that the minimum mass entering the pair instability regime reduces as the initial rotation velocity increases.

Once He is exhausted in the center, the CO core starts contracting again while the He burning shifts in a shell where a He convective shell forms. If mass loss did not erode the He core during the central He burning, or if the star did not rotate, the He convective shell forms above the He discontinuity left by the progressive advance of the convective core, in a region with a flat He

profile where no products of the He burning are present. Vice versa, if mass loss was efficient enough to erode the He core mass while the star was still in central He burning or rotation induced mixing modified the chemical composition of the intershell, the He convective shell forms in a region that has a pronounced He profile left over by either the receding He convective core (if the He core is reduced by mass loss) or determined by the continuous exchange of matter between the convective core an the H shell burning (in rotating models).

3.1.4 Advanced nuclear burning stages

The following section will describe the evolutionary properties of all the models that do not enter the pair instability regime. During advanced nuclear burning stages the rotation does not affect significantly the evolutionary properties of a star beyond the He burning because the timescales over which the rotation instabilities operate are much longer than the advanced evolutionary timescales, moreover the local gravity of the core dominates over the centrifugal force. Also the initial metallicity does not play any direct role in the physical evolution of a star in the advanced burning phases because all the relevant nuclear reactions involve primary nuclei. In other words the evolution of a star in the advanced burning phases is not linked any more to its initial mass, metallicity and initial rotation velocity, but it is controlled essentially by the mass of the CO core. The role of initial metallicity and rotation velocity influence the advanced burning only through their capability of modifying the mass of the CO core as well as the abundance of ^{12}C at the end of core He burning. Note that, in all models of the present grid, no convective region crosses the outer edge of the CO core, therefore the total angular momentum stored in the CO core will remain constant up to the onset of the iron core collapse.

3.2 SEVN code

In this section our population-synthesis code SEVN[1] will be presented (Spera et al., 2018).

SEVN evolves the physical parameters of stars by reading a set of tabulated stellar evolutionary tracks that are interpolated on-the-fly. The default version of SEVN includes look-up tables generated by PARSEC code (Chen et al., 2015), but in this work I added the look-up tables

[1] https://gitlab.com/sevn/SEVN

presented in section 3.1. To perform the interpolation, in SEVN we distinguish between stars that are on the main sequence (H phase) and stars have already formed a He core but not yet a CO core (He phase) and stars that have already formed a CO core (CO phase). The division into three macro-phases is convenient in terms of computing time and also ensures that the stars used for the interpolation have the same internal structure. Furthermore, we impose that the interpolating stars have the same percentage of life (Θ_P) of the interpolated star on its macro-phase. For every time t, the percentage of life of a star is:

$$\Theta_P = \frac{t - t_{0,p}}{t_{f,p} - t_{0,p}} \tag{3.1}$$

where $t_{0,p}$ is the starting time of the star's evolutionary macro-phase p and $t_{f,p}$ is its final time. By using Θ_P, we ensure that the stars used for the interpolation are the same stellar evolutionary phase within the same macro-phase. In addition to these three macro-phases, we have defined several stellar-evolution phases. Tab 3.2.1 shows the list of the stellar evolutionary phases and their corresponding macro-phases used in the SEVN code. The stellar evolution phase of a star is evaluated using the values and the rate of change of the interpolated physical stellar parameters. It is worth nothing that in SEVN we mark a star as Wolf-Rayet (WR, $k = 7,8,9$) if

$$\frac{|M - M_{He}|}{M} < 2 \times 10^{-2} \tag{3.2}$$

where M is the total mass of the star and M_{He} is its He-core mass.

As to single stellar evolution, SEVN to evolve a star s with ZAMS mass $M_{ZAMS,s}$ and metallicity Z_s at time t uses four interpolation tracks from the look-up tables. Two of them have metallicty $Z_1 = Z_s - \Delta Z$ and ZAMS masses $M_{ZAMS,1} = M_{ZAMS,s} - \Delta M$ and $M_{ZAMS,2} = M_{ZAMS,s} + \Delta M$, respectively, where ΔM is the step of the mass grid of the look-up tables at metallicity Z_1 and ΔZ is the step of the metallicity of the look-up tables. The other two interpolation tracks have ZAMS masses $M_{ZAMS,1}$ and $M_{ZAMS,2}$ and metallicity $Z_2 = Z_s + \Delta Z$. To begin with, we calculate the percentage of life Θ_p of the star s on its macro-phase p. Then, we use the interpolation tracks to calculate

$$M_{s,Z_j}(t) = \beta_1, M_{1,Z_j}(t_1, Z_j) + \beta_2, M_{2,Z_j}(t_2, Z_j) \tag{3.3}$$

k	Phase	Macro-phase
0	Low-mass main sequence (MS, M <0.7 $M_\odot$	H phase
1	MS (M >0.7 $M_\odot$)	H phase
2	Hertzsprung gap (HG)	He phase
3	First giant branch	He phase
4	Core He burning	He phase
5	Early asymptotic giant branch (AGB9	CO phase
6	Thermally pulsating AGB	CO phase
7	Naked Helium MS	He phase
8	Naked Helium HG	CO phase
9	Naked Helium giant branch	CO phase
10	He white dwarf (WD)	none
11	Carbon-Oxygen WD	none
12	Oxygen-Neon WD	none
13	Neutron Star (NS)	none
14	Black Hole (BH)	none
-1	Massless remnant	none

Table 3.2.1: List of the integer values k used for stellar evolutionary phases and their corresponding macro-phases. A naked Helium MS is a naked Helium star burning Helium in the core. A naked Helium HG is a naked Helium star burning Helium in shells. A naked Helium giant branch is a naked Helium star burning Carbon (or a heavier element) in the core.

where

$$t_i, Z_j \equiv \Theta_p(t_{f,p,i,Z_j} - t_{0,p,i,Z_j}) + t_{0,p,i,Z_j},$$

$$\beta_1 \equiv [M_{ZAMS,1}(M_{ZAMS,2} - M_{ZAMS,s})]/[M_{ZAMS,s}(M_{ZAMS,2} - M_{ZAMS,1})],$$

$$\beta_2 \equiv [M_{ZAMS,}(M_{ZAMS,s} - M_{ZAMS,1})]/[M_{ZAMS,s}(M_{ZAMS,2} - M_{ZAMS,1})],$$

$i, j \in [1, 2]$ and $t_{0,p,i,Z_j}(t_{f,p,i,Z_j})$ is the starting (end) time of the macro-phase p of the star with ZAMS mass M_i at metallicity Z_j. The use of the β_1 and β_2 weights allows us to keep the interpolation error below 1% with respect to the original evolutionary track and to include less points in the look-up tables. We calculate the interpolated value of the mass of the star s at time t as

$$M_s(t) = \gamma_1 M_{s,Z_1}(t) + \gamma_2 M_{s,Z_2}(t), \tag{3.4}$$

where $\gamma_1 \equiv (Z_s - Z_1)/(Z_2 - Z_1)$ and $\gamma_2 \equiv (Z_2 - Z_s)/(Z_2 - Z_1)$.

To evolve the mass of a star from time t_1 to time $t_2 = t_1 + \Delta t$, we use the formula

$$M_2 = M_1 + V_m M1 \tag{3.5}$$

where $V_m = (m_2 - m_1)/m_1$. In the above formula M_2 is the mass of the star at time t_2, M_1 is the mass of the star at time t_1, m_1 and m_2 are the masses of the star obtained from the interpolation tracks at time t_1 and t_2, respectively, and V_m is the relative variation of the mass of the star, calcualted from the interpolation tracks. We use equation 3.5 because, should the track-finding algorithm not converge, the temporal evolution of M is still continuous. In contrast, if the track-finding algorithm converges, we have $M_1 \simeq m_1$, that is $M_2 \simeq m_2$, which means that the evolution of the star is synchronous with the values in the look-up tables. We adopt the same technique for the temporal evoultion of M_{He}, and M_{CO}, while we keep R, L and time always sinchronous with the values obtained with the interpolation tracks.

3.2.1 Prescriptions for supernovae (SNe)

The prescription for SNe adopted in SEVN are five:

1. rapid core-collapse model (Fryer et al., 2012)
2. delayed core-collapse model (Fryer et al., 2012)
3. the prescription implemented in the STRARTRACK code (Belczynski et al., 2010)
4. a model based on the compactness parameter (O'Connor and Ott, 2011)
5. the two-parameters criterion (Ertl et al., 2016)

In this thesis work I used only the first two models, the rapid and delayed core-collapse.

In order to calculate the mass of the remnant with the rapid explosion mechanism we need the mass of the star M, the mass of the CO core (M_{CO}) at the time of the core-collapse/SN explosion. The PNS mass (M_{PNS}) is fixed at 1 $M_\odot$, while the mass of the fallback M_{fb} is obtained based on

M_{CO}:

$$\begin{cases} M_{fb} = 0.2 M_\odot & M_{CO} < 2.5 M_\odot \\ M_{fb} = 0.286 M_{CO} - 0.514 M_\odot & 2.5 \leq M_{CO} < 6.0 M_\odot \\ f_{fb} = 1.0 & 6.0 \leq M_{CO} < 7.0 M_\odot \\ f_{fb} = a_1 M_{CO} + b_1 & 7.0 \leq M_{CO} < 11.0 M_\odot \\ f_{fb} = 1.0 & M_{CO} \geq 11.0 M_\odot \end{cases}$$

with $a_1 = 0.25 - 1.275/(M - M_{PNS})$, $b_1 = -11 a_1 + 1$ and $M_{fb} = f_{fb}(M - M_{PNS})$ in the mass range for which f_{fb} is given.

The final baryonic mass of the remnant is $M_{rem,bar} = M_{PNS} + M_{fb}$. The delayed explosion mechanism is similar to the rapid. However in this case M_{PNS} is not fixed

$$\begin{cases} M_{PNS} = 1.2 M_\odot & M_{CO} < 3.5 M_\odot \\ M_{PNS} = 1.3 M_\odot & 3.5 \leq M_{CO} < 6.0 M_\odot \\ M_{PNS} = 1.4 M_\odot & 6.0 \leq M_{CO} < 11.0 M_\odot \\ M_{PNS} = 1.6 M_\odot & M_{CO} \geq 11.0 M_\odot \end{cases}$$

This assumes that the delay increases for more massive cores, causing more material to accrete onto the proto-neutron star during the explosion. The amount of fallback is given by

$$\begin{cases} M_{fb} = 0.2 M_\odot & M_{CO} < 2.5 M_\odot \\ M_{fb} = 0.5 M_{CO} - 1.05 M_\odot & 2.5 \leq M_{CO} < 3.5 M_\odot \\ f_{fb} = a_2 M_{CO} + b_2 & 3.5 \leq M_{CO} < 11.0 M_\odot \\ f_{fb} = 1.0 & M_{CO} \geq 11.0 M_\odot \end{cases}$$

with $a_2 = 0.133 - 0.093/(M - M_{PNS})$, $b_2 = -11 a_2 + 1$ and $M_{fb} = f_{fb}(M - M_{PNS})$ in the mass range for which f_{fb} is given. The final baryonic mass of the remnant is $M_{rem,bar} = M_{PNS} + M_{fb}$.

At last the final baryonic mass is converted in gravitational mass (M_{rem}) using

$$M_{rem,bar} - M_{rem} = 0.075 M_{rem}^2$$

for NS, while for BH

$$M_{rem} = 0.9 M_{rem,bar}.$$

4

Results

In this section I will present the results obtained in my thesis.

Based on the theoretical background and the models presented in the previous chapters, the effects of rotation can be summarised in two main consequences: the increase in luminosity and the more efficient chemical mixing. The first leads to an enhancement of stellar winds, while the latter tends to create heavier stellar cores with respect to the non rotational models. These two processes are against one another, as a matter of fact the enhanced stellar winds leads to the creation of lighter remnants, while the heavier core results in more massive compact objects. It is essential to understand which process dominate over the other and which parameters influence the most the outcome of simulations. On top of all that, PISNe complicate even more the scenario: if the mass of the core grows too much the star will be completely destroyed.

Before explaining in details the simulations I will present some of the preliminar work done on the models.

4.1 Interpolation of the FRANEC models

SEVN reads pre-evolved stellar evolution tracks, generated from a grid of ZAMS masses, different metallicities and initial equatorial velocities to calculate the physical properties of the stars. Stellar tracks are given in the form of input tables that SEVN interpolates on-the-fly. This approach is possibile with the FRANEC models only after a conversion of the grids. The models presented here[1] need to be rearranged in a way that makes them readable from SEVN, in order to do so I converted all the tracks into matrices usable by SEVN. In figure 4.1.1, 4.1.2, 4.1.3 are plotted some examples of the conversion I made; in particular figure 4.1.1 shows the star mass as a function of time, in the top panel, and the logaritmic star radius as a function of time, in the bottom one. The blue stars used as markers represent the actual values taken from the matrices usable by SEVN. In figure 4.1.2, where there is the time evolution of the mass (top) and the radius (bottom) of the helium core, there is a gap between the two lines in the top panel: it is not a mistake, it is a precise choice made for this kind of star. As a matter of fact a star with the initial condition under discussion (40 $M_{\odot}$, [Fe/H]=0 and V_{eq} = 300 Km/s) enters the WR stage, in which almost all the mass of the star is the mass of its He core. Thus, after the H burning shell disappears due to stellar winds, there is no more a He core, but only a He star. In figure 4.1.3 the top panel shows the mass of the CO core as a function of time, as can be seen the blue interpolation does not follow the black model. Also this is the outcome of a choice: FRANEC marks as CO core everything inside the He burning shell, the fluctuations in the mass are only the result of a fluctuation of the radius at which the He burning shell is located. For this reason we chose to maintain the CO core mass stable during the conversion of the models. In figure 4.1.4 all the masses of all the components of the star are plotted as a function of time, as it can be observed as the star enters the WR stage all its mass is composed of its helium core.

[1] http://orfeo.iaps.inaf.it/

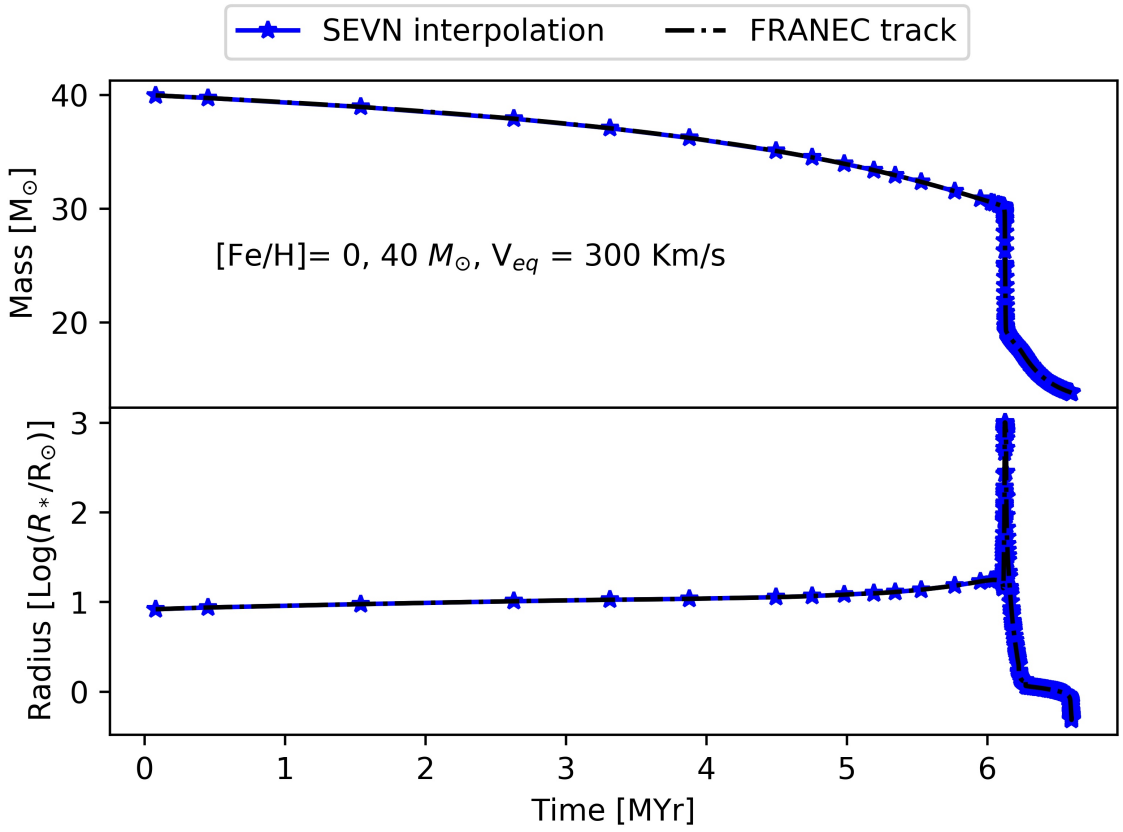

Figure 4.1.1: In the top panel is represented the mass of a 40 $M_\odot$ star with metallicity [Fe/H]=0 and initial equatorial velocity V_{eq} = 300 Km/s as a function of time. The black line is the original FRANEC model, while the blue line represents the converted matrix. The marker stars represent values that belong to the matrix, as shown they are more dense where the star evolves more rapidly. In the bottom panel the logaritmic radius of the star is plotted as a function of time, the color scheme is the same as the panel above. The interpolation of the models is made with an error of a part in a thousand.

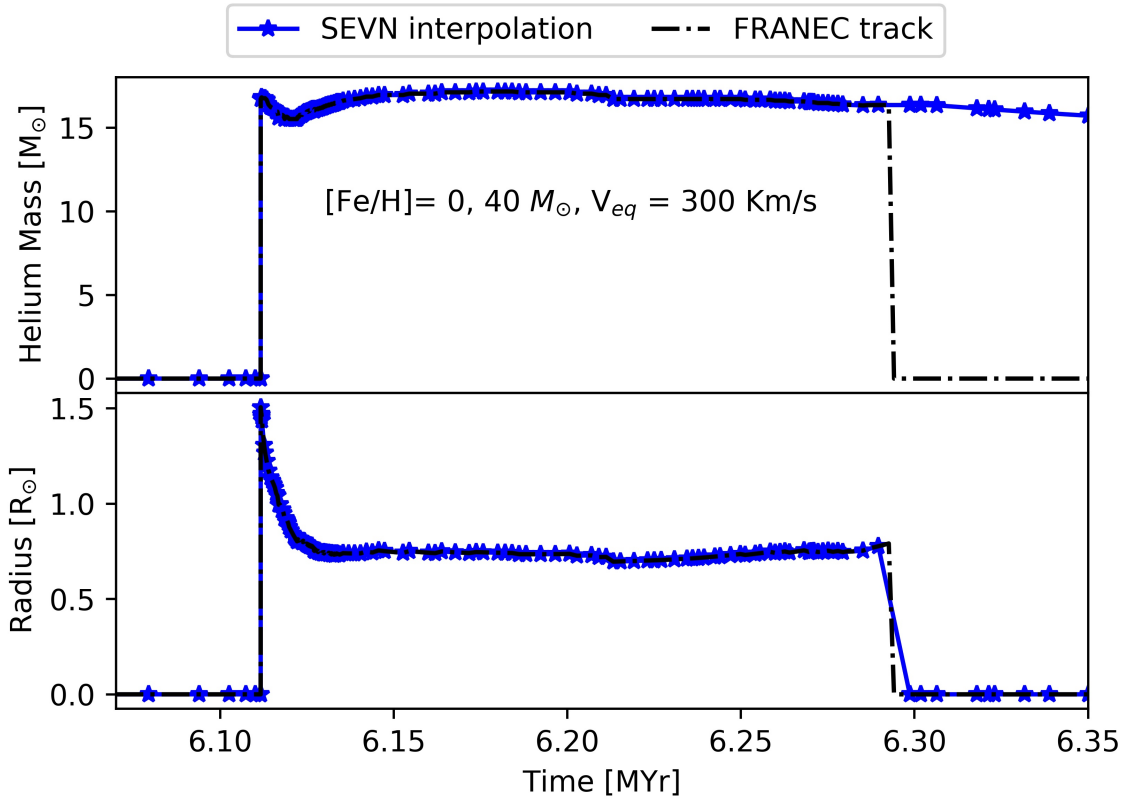

Figure 4.1.2: In the top panel the mass of the helium core of a 40 $M_\odot$ star with metallicity [Fe/H]=0 and initial equatorial velocity V_{eq} = 300 Km/s is represented as a function of time. The black line is the original FRANEC model, while the blue line represents the converted matrix. The marker stars represent values that belong to the matrix, as shown they are more dense where the star evolves more rapidly. The bottom panel shows the radius of the helium core as a function of time.

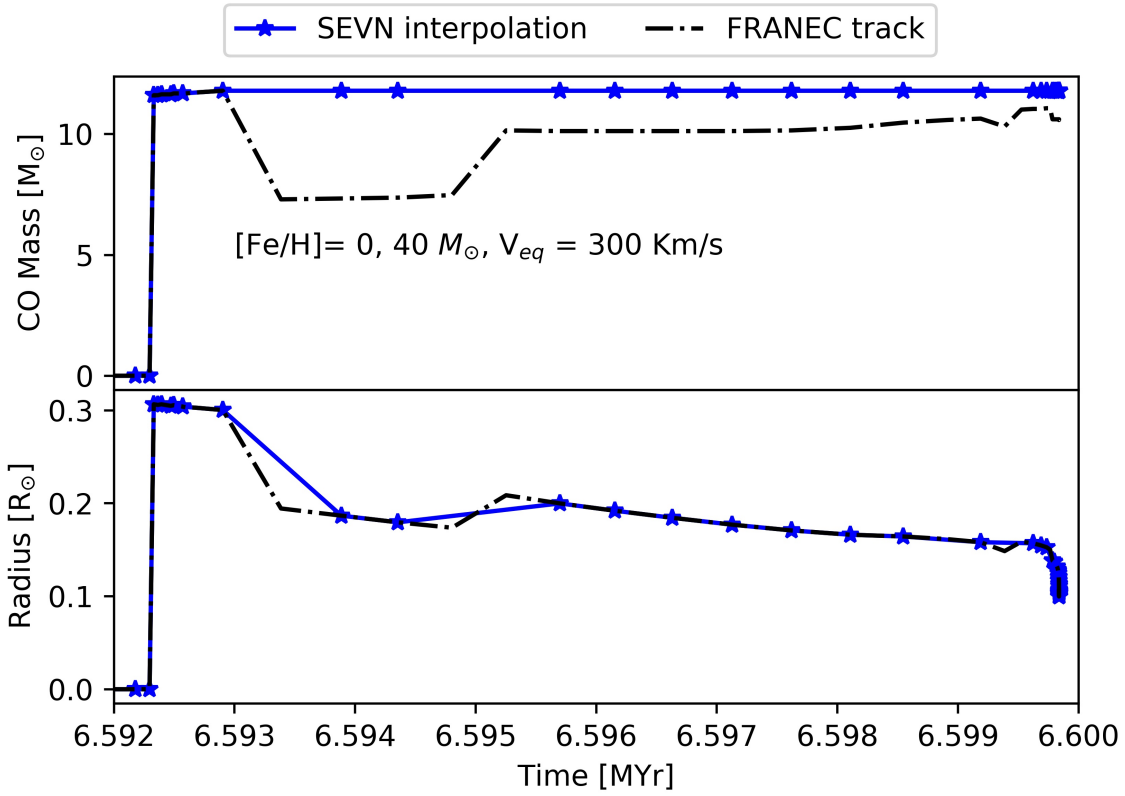

Figure 4.1.3: In the top panel the mass of the carbon-oxygen (CO) core of a 40 $M_\odot$ star with metallicity [Fe/H]=0 and initial equatorial velocity $V_{eq} = 300$ Km/s is represented as a function of time. The black line is the original FRANEC model, while the blue line represents the converted matrix. The marker stars represent values that belong to the matrix, as it can be observed they are more dense where the star evolves more rapidly. The bottom panel shows the radius of the CO core as a function of time.

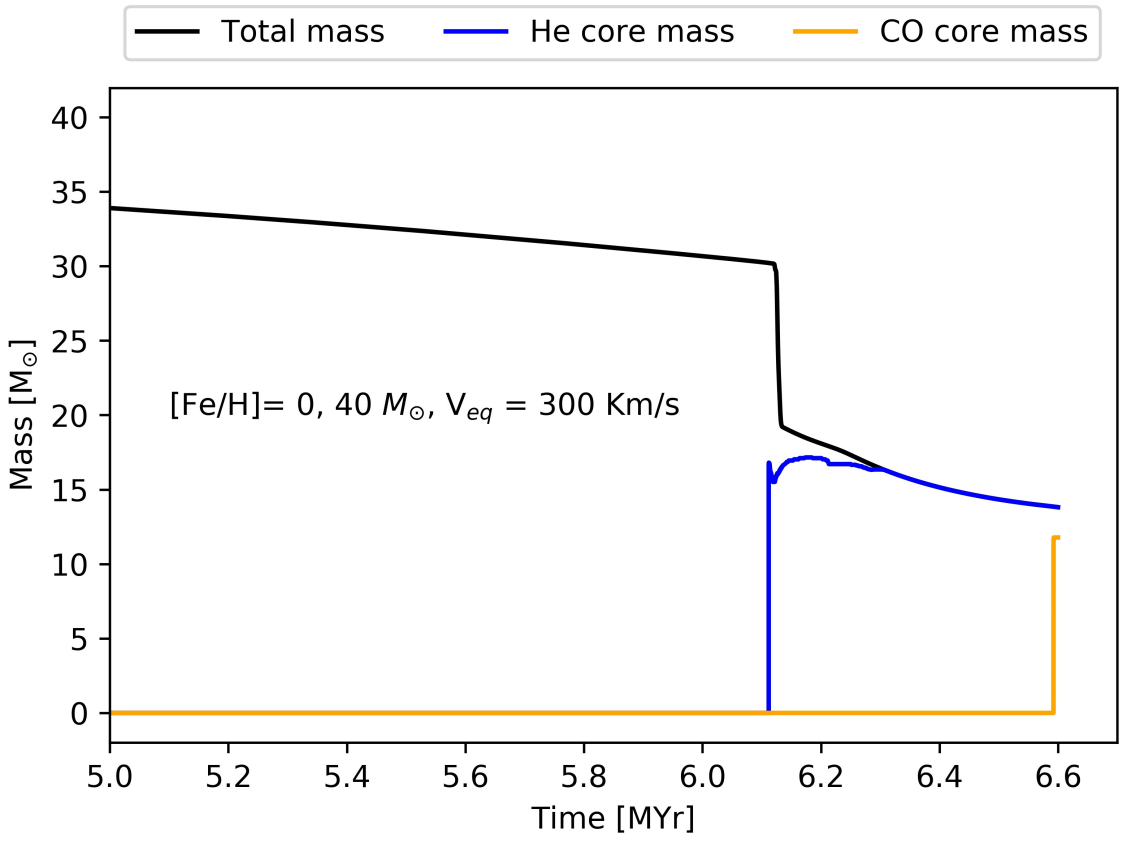

Figure 4.1.4: In this figure the total mass of the star, represented in black, the mass of the helium core, represented in blue, and the CO core mass represented in orange are plotted as a function of time. It can be seen that a tiny fraction of the He core mass survives as a shell unti the end of the life of the star.

4.2 The influence of rotation on stellar winds

Stellar rotation influences stellar winds enhancing star's luminosity. A visual representation of this effect can be seen in a Hertzsprung-Russel (HR) diagram; in 4.2.1 the evolution track of a 13 $M_{\odot}$ star is represented with different initial equatorial velocities (V_{eq}). If the red line (V_{eq}=300 km/s) lies above the black one (V_{eq}= 0 km/s), then it will indicate that the rotating star is more luminous than the non rotating one, as predicted. Moreover the enhanced luminosity leads to more effective stellar winds, thus more mass loss. In figure 4.2.2 this effect can be seen in the top panel, where a 13 $M_{\odot}$ star is plotted as a function of time. The different initial velocity leads to a different evolution in time, in fact the model with null initial velocity (black line) ends its life earlier with respect to other models and with a higher final mass ($\sim$ 12 $M_{\odot}$ against $\sim$ 5 $M_{\odot}$). The extended lifetime is due to a better internal chemical mixing which leads to a larger core. Furthermore enhanced mass loss drives the star in a different stage: the rotating star enters the BSG stage, while the non rotating one remains a RSG. In the bottom panel of figure 4.2.2 a 40 $M_{\odot}$ star is plotted as a function of time, in this case the effect of different mass loss can be only noticed thanks to the slight mass difference before the steep mass drop.

4.3 The influence of rotation on chemical mixing

Stellar rotation influences also chemical mixing and two visible effects of this fact are a prolonged lifetime and the creation of more massive core. Regarding prolonged lifetime, it is clear in figure 4.2.2 that the rotating star has a longer lifetime with regards to the non rotating counterpart. As mentioned before, this effect holds for different masses: the top panel represents a 13 $M_{\odot}$, while the bottom one represents a 40 $M_{\odot}$. This general trend holds also at different metallicities. Figure 4.3.1 shows the time evolution of a 13 $M_{\odot}$ star, in the top panel, while the bottom one represents a 40 $M_{\odot}$. Both plots show models at $\left[Fe/H\right]$=-3 and have a black solid line for the non rotating model while the dotted red line stands for the rotating one. With such a low metallicity stellar winds are almost negligible, thus, the better chemical mixing leads to a longer lifetime for rotating stars.

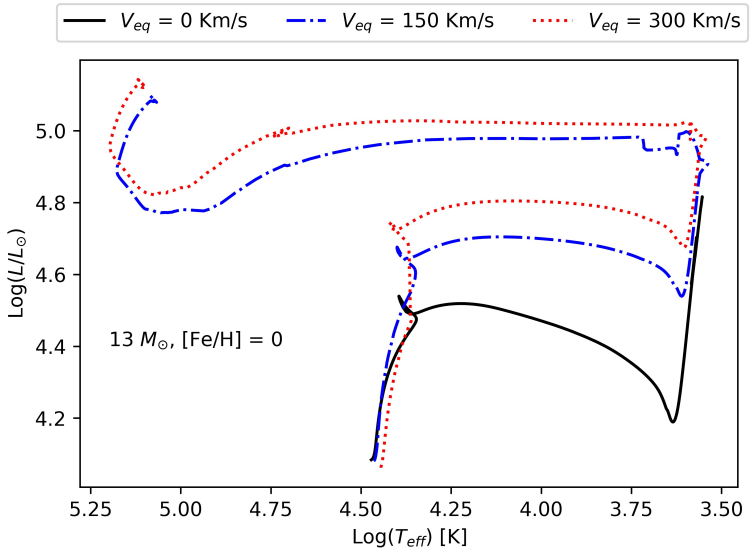

Figure 4.2.1: Evolutionary tracks of a 13 $M_\odot$ star at solar metallicity, but with different equatorial velocity. The color scheme is the same as figures 4.1.4 and 4.2.2; the x axis represents the effective temperature logarithm, while the y axis represents the star's luminosity over solar luminosity logarithm.

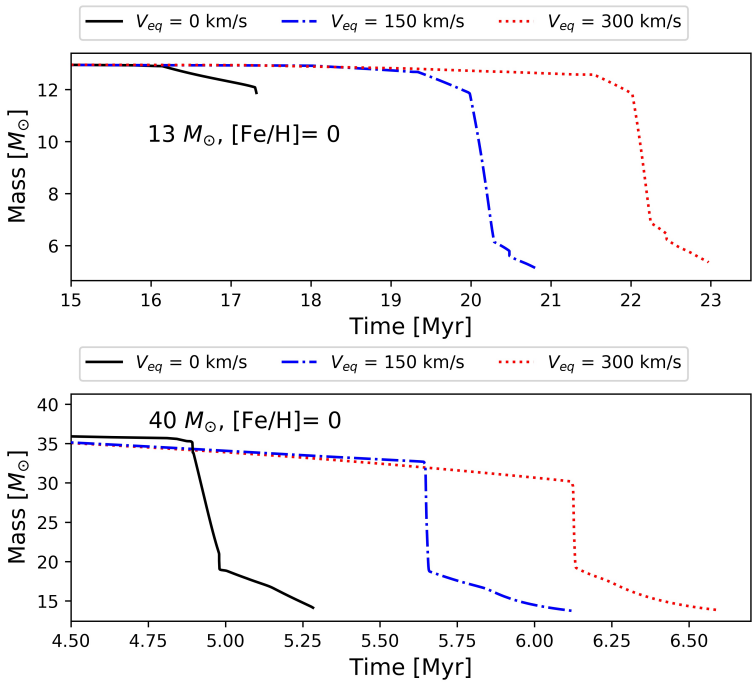

Figure 4.2.2: Mass of a 13 $M_\odot$ star (top panel) and a 40 $M_\odot$ star (bottom panel) are plotted against time; the black, blue and red line refer to different initial equatorial velocity, respectively 0 km/s, 150 km/s and 300 km/s. All the models plotted are at solar metallicity.

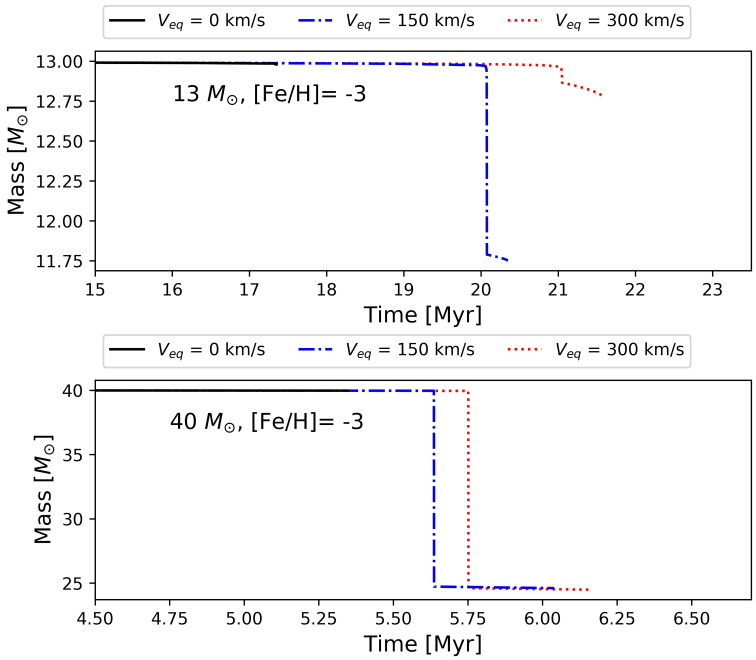

Figure 4.3.1: Time evolution of the total mass of a star at different velocities. Top panel shows a 13 $M_\odot$ star, while the bottom one describes a 40 $M_\odot$ star. The black solid line represents the non rotating models, while the blue and red represent the rotating ones respectively the 150 and 300 km/s.

Speaking about the growth of a more massive helium core, figures 4.3.2 and 4.3.3 highlight how this effect is given thanks to a better chemical mixing. In particular this effect is more emphasised in the top panel of figure 4.3.2 where the 13 $M_{\odot}$ rotating star develops an helium core $\sim$1 $M_{\odot}$ heavier than the non rotating counterpart. In the bottom panel of figure 4.3.2 the intense mass loss quenches the growth of the core, while, at $[Fe/H]$=-3 (figure 4.3.3), the 40 $M_{\odot}$ rotating star grows a core $\sim$ 5 $M_{\odot}$ heavier than the non spinning one. The difference between the two metallicities plotted is caused by the negligible mass loss at low metallicity.

Since the helium core grows heavier, also the carbon-oxygen core can reach higher masses. As explained in section 3.2.1, the prescriptions for CCSNe in SEVN use M_{CO} to calculate M_{remn}, thus a higher M_{CO} should result in a heavier M_{remn}. This trend can be seen in figures 4.3.4 and 4.3.5: the models at solar metallicity suffer the effect of stellar winds, in particular the 40 $M_{\odot}$, that almost doubles M_{CO} from $[Fe/H]$=0 to $[Fe/H]$=-3.

From all the diagrams presented so far, it is clear that the effect of rotation already saturates at 150 km/s; as a matter of fact there are huge differences between the models with 0 km/s and 150 km/s, while the 150 km/s and the 300 km/s model are similar.

4.4 Effects of rotation on BHs formation

In order to study the effect of rotation on BHs formation I analyzed the outcome of different sets of simulations, which initial conditions (IC) are listed in table 4.4.1. 24 simulations have been performed in total, I used three different velocities at each of the four metallicities for every SN explosion mechanism. Every set evolved 214 single stars in the range of masses mentioned above. Considering that all stars are isolated, two identical stars evolve in the same way, thus it was pointless to run the same ICs more than once.

Based on the results highlighted in sections 4.2 and 4.3, I will now present the effects of rotation on the formation of stellar BHs. The general tendency is to create heavier cores at higher initial equatorial velocities as the metallicity decreases. This trend holds as long as we do not consider PPISNe and PISNe (see section 2.3). As a matter of fact, if the helium core grows above $\sim$30 $M_{\odot}$ pulsational instability becomes effective causing mass loss, while at 64 $M_{\odot}$ the disruptive

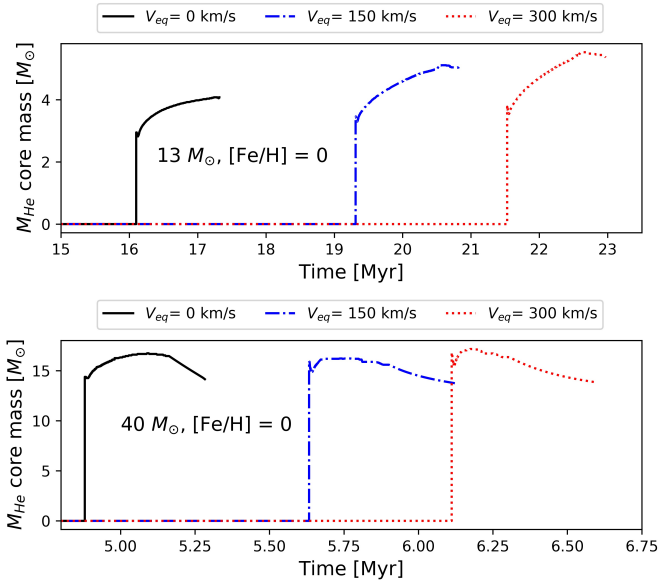

Figure 4.3.2: Time evolution of the helium core mass of a 13 $M_\odot$ star (top panel) and a 40 $M_\odot$ star (bottom panel) with 0 km/s (solid black line), 150 km/s(dash dot blue line) and 300 km/s (dotted red line), every the models have solar metallicity.

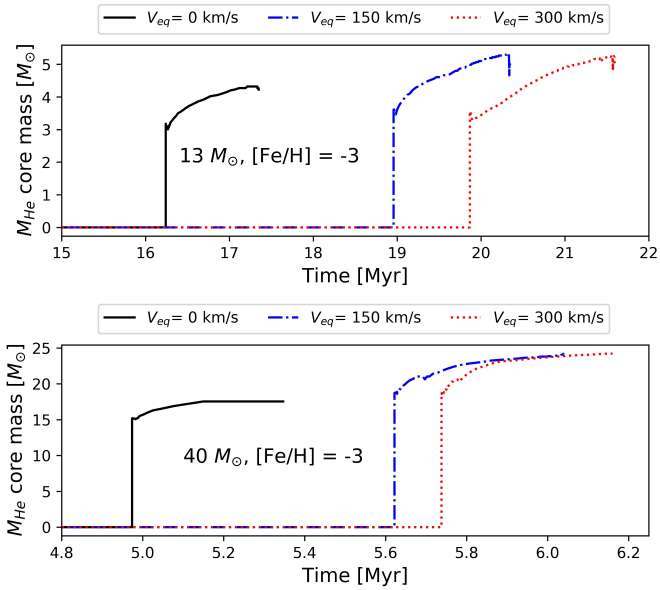

Figure 4.3.3: Time evolution of the helium core mass of a 13 $M_\odot$ star (top panel) and a 40 $M_\odot$ star (bottom panel) with 0 km/s (solid black line), 150 km/s(dash dot blue line) and 300 km/s (dotted red line), every the models have 1/1000 solar metallicity.

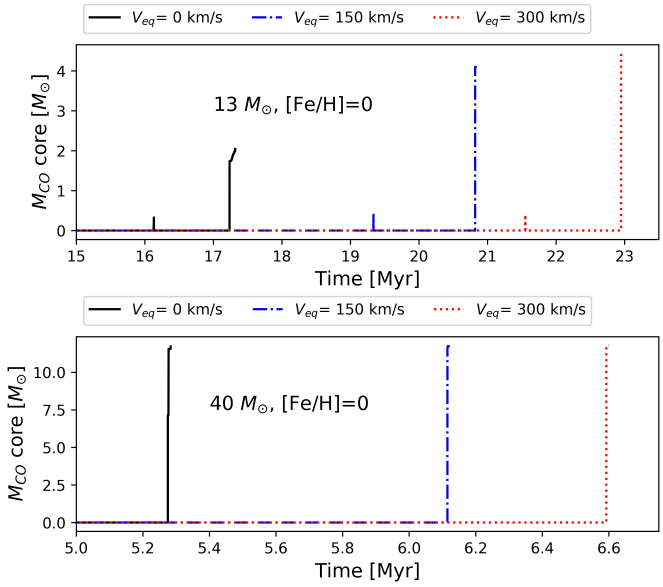

Figure 4.3.4: Time evolution of CO core mass (M_{CO}) of a 13 $M_\odot$ star (top panel) and a 40 $M_\odot$ star (bottom panel) with 0 km/s (solid black line), 150 km/s (dash dot blue line) and 300 km/s (dotted red line), every the models have solar metallicity.

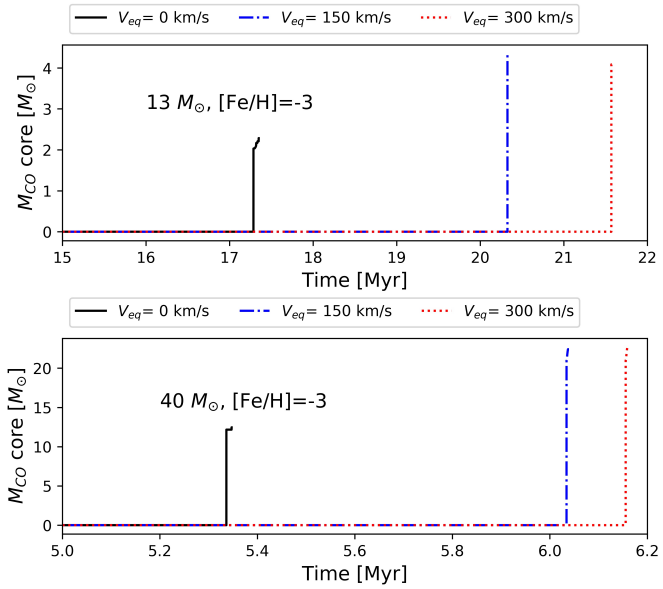

Figure 4.3.5: Time evolution of CO core mass (M_{CO}) of a 13 $M_\odot$ star (top panel) and a 40 $M_\odot$ star (bottom panel) with 0 km/s (solid black line), 150 km/s (dash dot blue line) and 300 km/s (dotted red line), every models have 1/1000 solar metallicity.

Parameter	Value
$[Fe/H]$	0, -1, -2, -3
$M_{ZAMS}\,[M_\odot]$	$13 \leq m \leq 120$
$V_{eq,ini}\,[km/s]$	0, 150, 300
SNe mechanism	rapid/delayed

Table 4.4.1: Sets of initial conditions used in SEVN. The initial metallicity spanned from solar metallicity to 1/1000 solar metallicity; M_{ZAMS} covered a range of values from 13 $M_\odot$ to 120 $M_\odot$ with a step of 0.5 $M_\odot$; the used initial equatorial velocities of the stars were 0, 150 and 300 km/s; the SN mechanisms used were the delayed and the rapid (Fryer et al., 2012).

mechanism of the pair instability takes place leaving no remnant. Figures 4.4.1 and 4.4.2 well illustrate this scenario: at solar metallicity, enhanced stellar winds prevail over everything else, thus the helium core is not able to grow and M_{rem} does not reach $30M_\odot$. At subsolar metallicity, as the stellar winds keep to decline, the effects of the chemical mixing are shown in the form of heavier cores. In figure 4.4.2, the rotating stars grow helium cores heavy enough to trigger PISNe, and as a result they leave no remnant; the non rotating models cannot grow such heavy cores and, thus, they enter the pulsational instability developing lighter remnants.

In order to have a global overview of the results obtained in this work, figures 4.4.5 and 4.4.6 presents all the M_{ZAMS} vs M_{rem} plots, showing dependencies from metallicity and from CCSN explosion models. Before going into detail of the masses obtained, the differences between the rapid model (figure 4.4.6) and delayed model (figure 4.4.5) can be seen only at low mass. Using the delayed mechanism M_{rem} gradually grows, passing from NS to BH smoothly; quite the opposite happens with the rapid mechanism, in which M_{rem} abruptly grows with M_{ZAMS}.

Finally, the maximum masses obtained for the remnant are heavily influenced by the PISNe process, as a consequence the rotating models develops lighter remnant with respect to the non rotating one. As mentioned above, the main differences appear between rotating and non rotating models: the mass of the BH are similar if we only look at rotating stars.

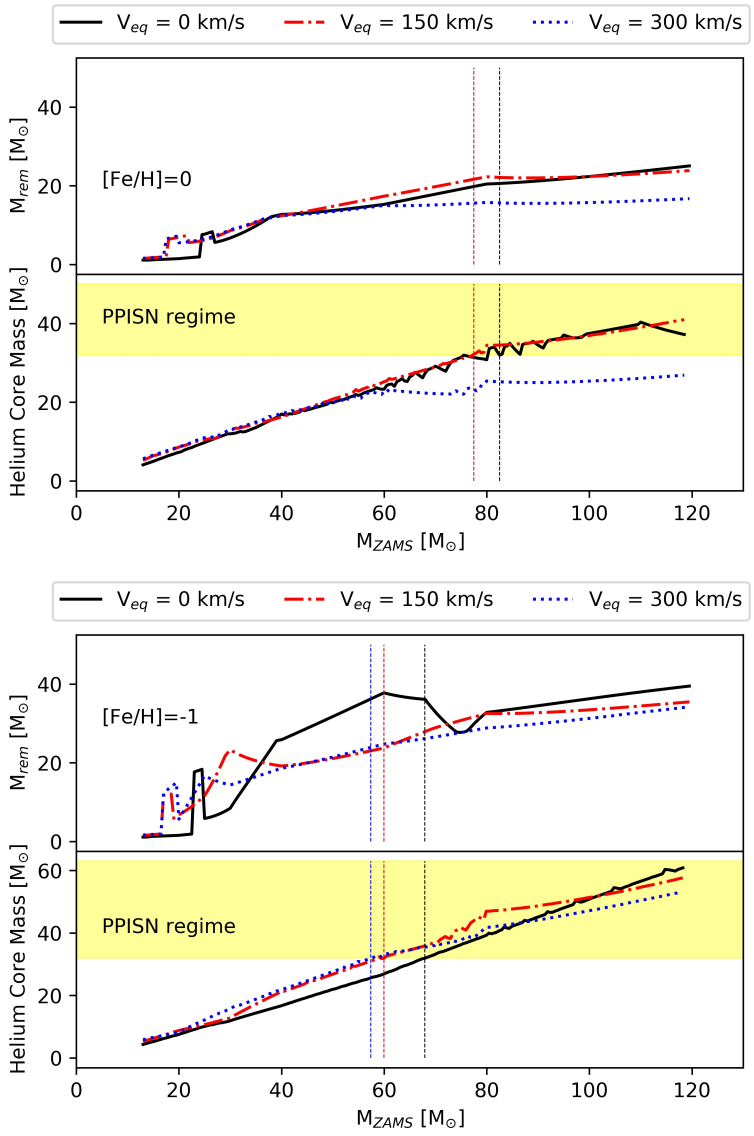

Figure 4.4.1: Both figures show the mass of the compact object (M_{rem}) as a function of the ZAMS mass (M_{ZAMS}), in the top panel, while in the bottom one the mass of the helium core (M_{He}) is expressed in relation with M_{ZAMS}. The color/style scheme is the same of the previous images, while the dashed vertical lines mark where the helium core grows above 32 solar masses. The upper figure is at solar metallicity, the lower at 1/10 solar metallicity. The explosion model used here was the rapid one.

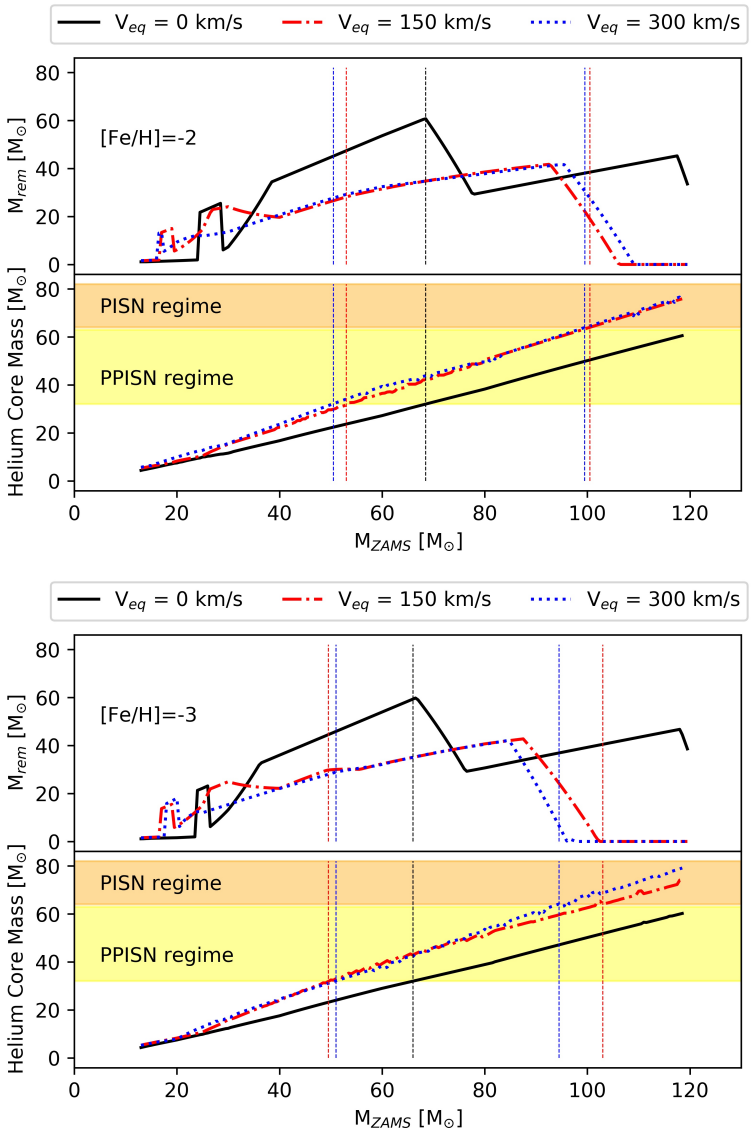

Figure 4.4.2: Both figures show the mass of the compact object (M_{rem}) as a function of the ZAMS mass (M_{ZAMS}), in the top panel, while in the bottom one the mass of the helium core (M_{He}) is expressed in relation with M_{ZAMS}. The color/style scheme is the same of the previous images, while the dashed vertical lines mark where the helium core grows above 32 (black) or 64 (blue and red) solar masses. The upper figure is at 1/100 solar metallicity, the lower at 1/1000 solar metallicity. The explosion model used here was the rapid one.

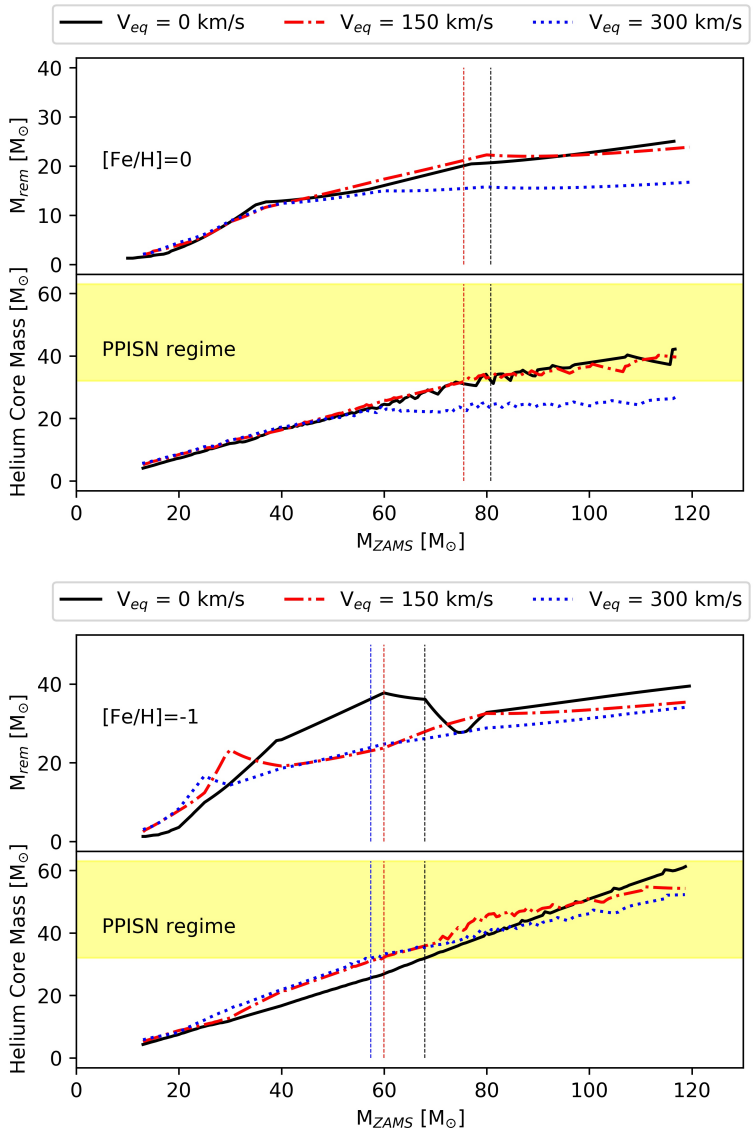

Figure 4.4.3: Both figures show the mass of the compact object (M_{rem}) as a function of the ZAMS mass (M_{ZAMS}), in the top panel, while in the bottom one the mass of the helium core (M_{He}) is expressed in relation with M_{ZAMS}. The color/style scheme is the same of the previous images, while the dashed vertical lines mark where the helium core grows above 32 solar masses. The upper figure is at solar metallicity, the lower at 1/10 solar metallicity. The explosion model used here was the rapid one.

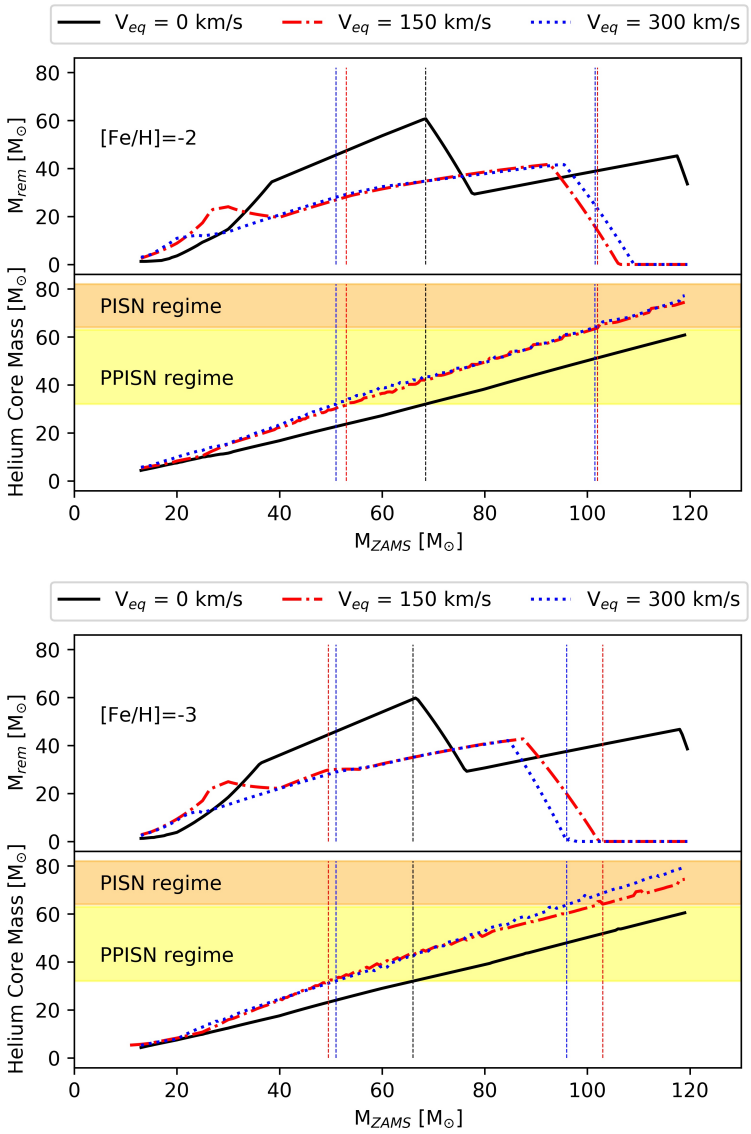

Figure 4.4.4: Both figures show the mass of the compact object (M_{rem}) as a function of the ZAMS mass (M_{ZAMS}), in the top panel, while in the bottom one the mass of the helium core (M_{He}) is expressed in relation with M_{ZAMS}. The color/style scheme is the same of the previous images, while the dashed vertical lines mark where the helium core grows above 32 (black) or 64 (blue and red) solar masses. The upper figure is at 1/100 solar metallicity, the lower at 1/1000 solar metallicity. The explosion model used here was the rapid one.

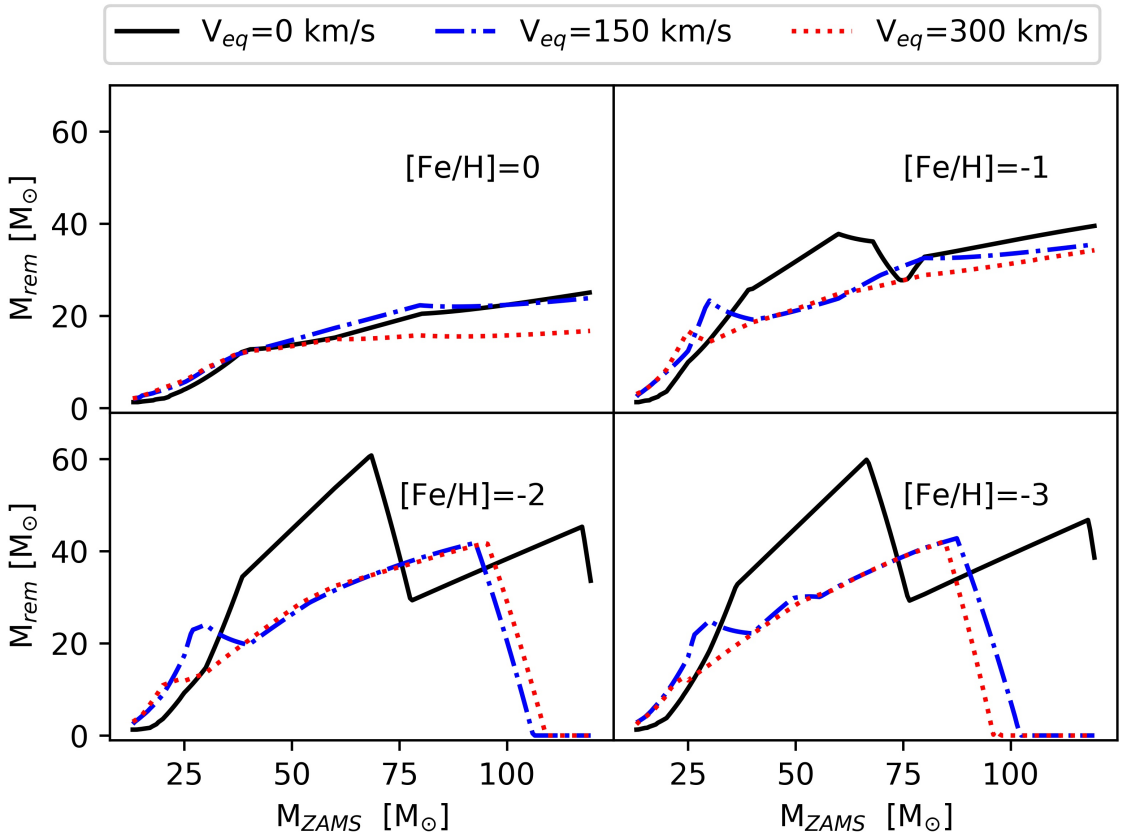

Figure 4.4.5: Remnant mass as a function of ZAMS mass M_{ZAMS}. Each panel portrays a different metallicity. Top row: [Fe/H]=0 and [Fe/H]=-1; bottom row: [Fe/H]=-2 and [Fe/H]=-3. Remnant masses obtained with the CCSN delayed model.

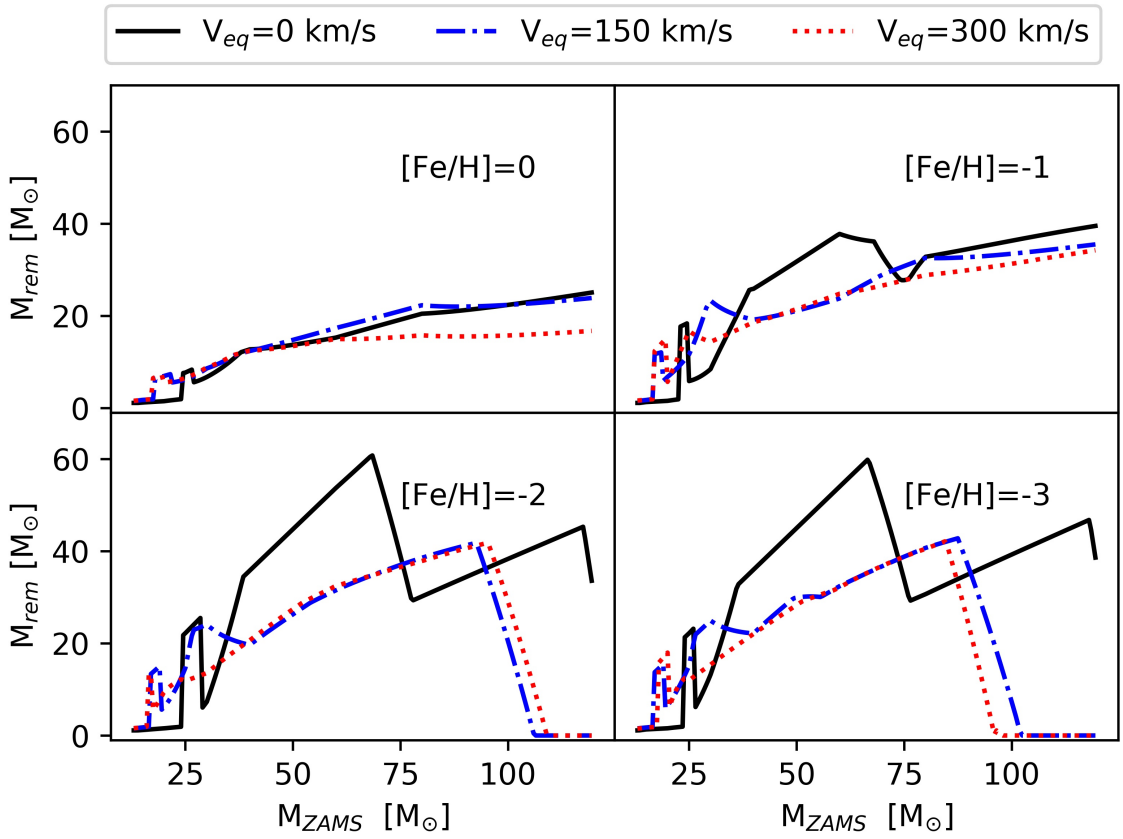

Figure 4.4.6: Remnant mass as a function of ZAMS mass M_{ZAMS}. Each panel portrays a different metallicity. Top row: [Fe/H]=0 and [Fe/H]=-1; bottom row: [Fe/H]=-2 and [Fe/H]=-3. Remnant masses obtained with the CCSN rapid model.

Table 4.4.2: Maximum mass of the BHs obtained. The mass grows with V_{eq} and for decreasing metallicity.

[Fe/H]	Initial equatorial velocity V_{eq}		
	0 km/s	150 km/s	300km/s
0	25.04 $M_{\odot}$	23.85 $M_{\odot}$	16.75 $M_{\odot}$
-1	39.48 $M_{\odot}$	35.47 $M_{\odot}$	34.2 $M_{\odot}$
-2	60.7 $M_{\odot}$	41.7 $M_{\odot}$	41.6 $M_{\odot}$
-3	59.7 $M_{\odot}$	42.7 $M_{\odot}$	42 $M_{\odot}$

At last, in order to quantify the results, in figure 4.4.7 is shown the comparison with what obtained by Spera and Mapelli (2017). Only three metallicities are shown, instead of the usual four, because the models used in the previous paper lack the [Fe/H]=-3, nevertheless is clear that at low metallicity the predictions for M_{rem} (green line) is significantly higher. Moreover, from the shape of the curve, it can be inferred that the models in this work trigger PISNe thanks to the improved chemical mixing, while the one in literature suffers only PPISNe. Further investigation showed that the maximum mass obtained in Spera and Mapelli (2017) at [Fe/H] = -2 is of the order of 55 $M_{\odot}$, a comparison with the outcome of my simulations at the same metallicity with the rotating models, where the gap is wider, shows that the BHs are 24% lighter than before. This is a remarkable result and, if compared with GW datas (see 1.0.1, can create robust constrains on further interpretation.

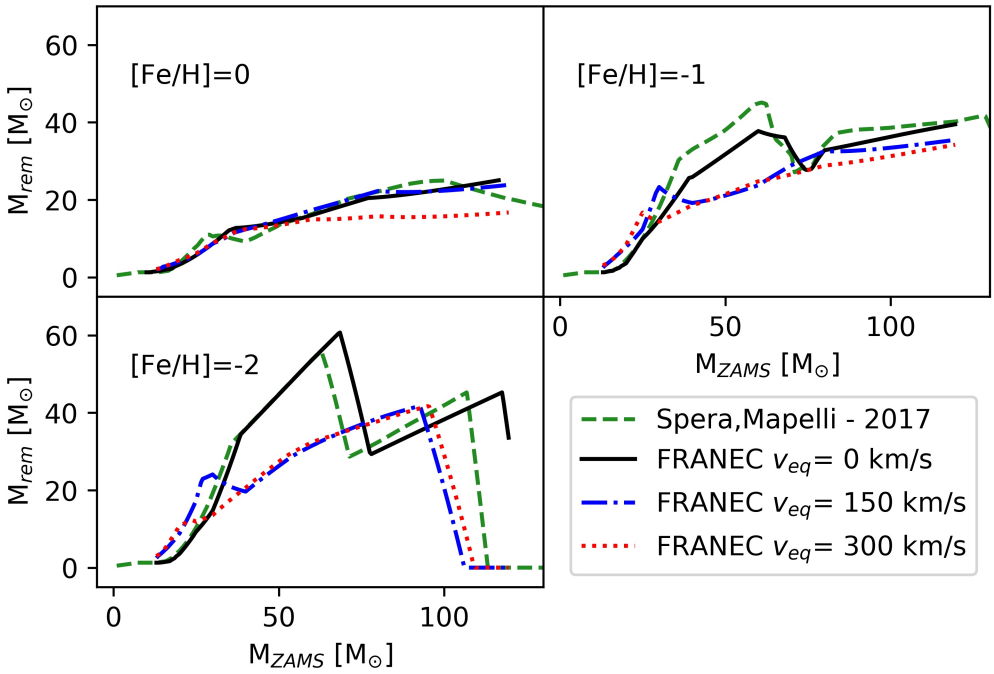

Figure 4.4.7: A comparison between the results obtained in this thesis, at three out of four metallicities, with Spera and Mapelli (2017). The lines represent the non rotating (solid black), the 150 km/s (dash dot blue), the 300 km/s model (dotted red) and the results of Spera and Mapelli (2017) (dashed green) at each metalicity. While in the top two panels the differences between all models are not so clear, in the bottom one is present a huge gap between the rotating models and the non rotating one.

5

Conclusions

In this thesis I studied the formation of NSs and stellar BHs from stars, focusing on different metallicity and different initial equatorial velocity.

I started analyzing the different FRANEC track to check the influence of rotation on the evolution of the star, such as the presence of more efficient stellar winds or the growth of larger cores. After this check, I interpolated the raw tracks in order to obtain grid of values of every parameter required by our population-synthesis code SEVN. Subsequently I ran a set of simulations aiming to fully explore the impact of each parameter of the original model, such as mass, velocity and metallicity. Moreover I tried to inquire the effects of the diverse CCSN prescription implemented in SEVN. Analyzing the outcome of the simulations, I obtained that rotation has a powerful effect on the formation of stellar BHs, in particular the difference between in BH mass rotating and non rotating models was $\sim 19\, M_{\odot}$. Since an in-depth study on the effect of rotation on the formation on BH has not been done yet, the result of this work is crucial to better interpret GW datas. Thank to this work we can now set new constrains on stellar BHs masses.

Future developments of this thesis could be using other CCSNe prescriptions, such as the one based on compactness, as well as the simulation of stars in binary systems. Moreover a more dense grid of tracks in the mass range could lead to more precise results in the mass of the BHs.

References

Abbott, B. P., Abbott, R., Abbott, T. D., Abernathy, M. R., Acernese, F., Ackley, K., Adams, C., Adams, T., Addesso, P., Adhikari, R. X., and et al. (2016). Astrophysical Implications of the Binary Black-hole Merger GW150914. , 818:L22.

Abbott, D. C. (1980). The theory of radiatively driven stellar winds. I - A physical interpretation. , 242:1183–1207.

Belczynski, K., Bulik, T., Fryer, C. L., Ruiter, A., Valsecchi, F., Vink, J. S., and Hurley, J. R. (2010). On the Maximum Mass of Stellar Black Holes. , 714:1217–1226.

Chen, Y., Bressan, A., Girardi, L., Marigo, P., Kong, X., and Lanza, A. (2015). PARSEC evolutionary tracks of massive stars up to 350 M at metallicities 0.0001 $\leq Z \leq$0.04. , 452 : 1068 — —1080.

Ertl, T., Janka, H. T., Woosley, S. E., Sukhbold, T., and Ugliano, M. (2016). A Two-parameter Criterion for Classifying the Explodability of Massive Stars by the Neutrino-driven Mechanism. , 818:124.

Fryer, C. L., Belczynski, K., Wiktorowicz, G., Dominik, M., Kalogera, V., and Holz, D. E. (2012). Compact Remnant Mass Function: Dependence on the Explosion Mechanism and Metallicity. , 749:91.

Limongi, M. and Chieffi, A. (2018). Presupernova Evolution and Explosive Nucleosynthesis of Rotating Massive Stars in the Metallicity Range -3 $\leq [Fe/H] \leq$0. , 237 : 13.

Maeder, A. (2009). *Physics, Formation and Evolution of Rotating Stars*. Springer.

Maeder, A. and Meynet, G. (2000). The Evolution of Rotating Stars. , 38:143–190.

Mapelli, M. (2018). Astrophysics of stellar black holes. *arXiv e-prints*, page arXiv:1809.09130.

O'Connor, E. and Ott, C. D. (2011). Black Hole Formation in Failing Core-Collapse Supernovae. , 730:70.

Spera, M. and Mapelli, M. (2017). Very massive stars, pair-instability supernovae and intermediate-mass black holes with the sevn code. , 470:4739–4749.

Spera, M., Mapelli, M., Giacobbo, N., Trani, A. A., Bressan, A., and Costa, G. (2018). Merging black hole binaries with the SEVN code. *arXiv e-prints*.

The LIGO Scientific Collaboration, the Virgo Collaboration, Abbott, B. P., Abbott, R., Abbott, T. D., Abraham, S., Acernese, F., Ackley, K., Adams, C., Adhikari, R. X., and et al. (2018). Binary Black Hole Population Properties Inferred from the First and Second Observing Runs of Advanced LIGO and Advanced Virgo. *arXiv e-prints*.

Vink, J. S., de Koter, A., and Lamers, H. J. G. L. M. (2001). Mass-loss predictions for O and B stars as a function of metallicity. , 369:574–588.

Woosley, S. E. (2017). Pulsational Pair-instability Supernovae. , 836:244.

Acknowledgments

Ringrazio infinitamente Michela Mapelli e Mario Spera per avermi aiutato nella stesura di questa tesi, per avermi spronato a migliorare, per avermi dato fiducia e per aver acceso in me la fiamma della passione per una carriera che non pensavo potesse essere la mia. Ringrazio tutti coloro che mi hanno accompagnato in questo lungo viaggio all'interno del mondo dell'università, durato più del previsto, ma goduto in ogni suo aspetto. Grazie a chi mi ha supportato moralmente in questo sforzo finale e grazie a chi ha dedicato parte del suo tempo per correggere e migliorare questa tesi. Grazie alla mia famiglia per tutto l'aiuto fornitomi. Ultimo, ma non meno importante, un sentito ringraziamento a Silvia, per essermi stata sempre accanto e non aver mai perso fiducia in me.